Cold Regions Science and Technology 217 (2024) 104042

Contents lists available at ScienceDirect

Cold Regions Science and Technology

journal homepage: www.elsevier.com/locate/coldregions

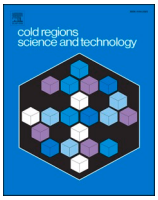

The potential for anti-icing wing and aircraft applications of mixed-wettability surfaces - A comprehensive review

S. Mahmood Mousavi [a,c], Freshteh Sotoudeh [a], Byoungjoo Chun [a], Bok Jik Lee [a,*], Nader Karimi [b], Salah A. Faroughi [c,*]

[a] Institute of Advanced Aerospace Technology, Seoul National University, Seoul 08826, Republic of Korea
[b] School of Engineering and Materials Science, Queen Mary University of London, London E1 4NS, United Kingdom
[c] Geo-Intelligence Laboratory, Ingram School of Engineering, Texas State University, San Marcos, TX 78666, USA

ARTICLE INFO

Keywords:
Anti-icing surfaces
Mixed wettability
Hydrophilic to superhydrophobic hybrid surfaces
Contact angle

ABSTRACT

The supercooled water droplets in clouds can cause ice to build up on the surfaces of aircraft and engines when planes are flying at low temperatures. The shape of the ice accretion depends on the temperature of the air, the liquid–water content of the air, the diameter of the droplets, the speed of the plane, and the phase of flight. The ice accretion reduces the plane's lift, increases the drag, and affects the stability. According to the National Transportation Safety Board (NTSB), icing of aircraft accounts for 12% of all in-flight weather-related incidents, and it can lead to huge losses. Thermal and mechanical techniques used to reduce ice formation often involve issues such as high energy consumption, environmental pollution, and high cost. Interestingly, an emerging approach involves the anti-icing treatment of surfaces by exploiting their wettability property. The surface micro/Nano texturing combined with the low surface energy of materials enhance the anti-icing properties. This article reviews the latest advancements in such approaches. Notably, the use of nature-material-based hydrophilic to superhydrophobic hybrid surfaces appears to offer a promising route to the suppression of ice accumulation and adhesion. Compared with uncoated surfaces, hybrid surfaces with high to low contact angles (mixed wettability) can not only delay the onset of ice formation effectively but also prolong the ice formation time. The mechanism by which hybrid surfaces reduce the residence time of liquid droplets and the wetted surface area is elucidated, and it is pointed out that such surfaces appear to be highly suitable for use in aircraft.

1. Introduction

During flight, airplanes may encounter the critical problem of icing, necessitating a deep understanding of the underlying concepts associated with this challenge (Poots et al., 1776). This perilous phenomenon, known as structural icing (Cole and Sand, 1991), arises under specific conditions: primarily, the aircraft must traverse through visible water sources, such as rain or cloud droplets. Secondly, the point at which the moisture strikes the aircraft's surface must register a temperature of 0 °C or colder (Antonini et al., 2011; Czernkovich, 2004). Intriguingly, even when the ambient temperature hovers slightly above this threshold, aerodynamic cooling can swiftly reduce the temperature of an airfoil to this critical point (Poots et al., 1776). The intricacy of this issue is further underscored by the presence of supercooled water, which remains liquid even below its freezing point (Moore and Molinero, 2011). When these supercooled droplets come into contact with an aircraft, a portion of the droplet solidifies immediately (Pérez-Díaz et al., 2016). This instantaneous phase change releases the latent heat of fusion, which then raises the temperature of the remaining liquid to its melting point (Meng and Zhang, 2020; Wang et al., 2023). Depending on aerodynamic conditions, this remaining liquid can then solidify (Papadakis et al., 2007). The unique process through which this freezing occurs is responsible for determining the specific type of icing that forms (Cebeci and Kafyeke, 2003). Another pivotal aspect to consider in this context is the 'liquid water content.' This term quantifies the volume of liquid water dispersed in the atmosphere, a metric that is subject to fluctuation based on prevailing atmospheric dynamics. It is noteworthy that certain locales are inherently more susceptible to high liquid water content — specifically, regions marked by elevated altitudes, extreme latitudes, and the cold embrace of winter (Jung et al., 2012; Marín et al., 2014; Schremb and Tropea, 2016). The ramifications of ice formation on an

Abbreviations: CA, contact angle; HS, hydrophilic surface; SHS, superhydrophobic surface; SC, Self-cleaning.

* Corresponding authors.
E-mail addresses: b.lee@snu.ac.kr (B.J. Lee), salah.faroughi@txstate.edu (S.A. Faroughi).

https://doi.org/10.1016/j.coldregions.2023.104042
Received 24 June 2022; Received in revised form 12 August 2023; Accepted 4 October 2023
Available online 10 October 2023

Nomenclature

C_T	thrust coefficient
D	diameter
F	critical force for contact line movement
t^*	nondimensional time (physical time/ characteristic time)
n	propeller's rotational speed
T	thrust force

Greek letters

α_m	area ratio: it is used to analyze the spread of a droplet on hydrophilic and hydrophobic regions at the moment of maximum spread
β_m	maximum spread factor
θ	Contact angle
θ_A	Advancing contact angle
θ_R	receding contact angle
γ_{lv}	liquid surface tension
ρ	density
Δθe	Defect strength, defined as the difference between the wall contact angles of the main surface and the stripe on a section of the surface.

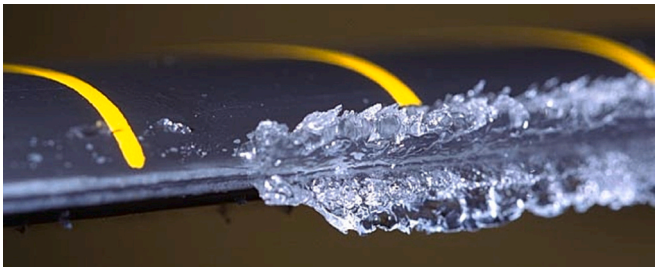

Fig. 1. Aerodynamic shape change of an aircraft wing resulting from ice formation on the wing (Fortin and Perron, 2009).

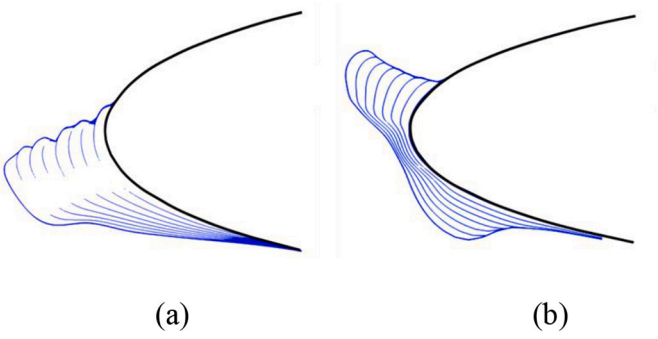

Fig. 2. (a) Rime ice at an ambient temperature of 245.35 K, and (b) Glaze ice at an ambient temperature of 265.71 K on a NACA 0012 airfoil at an angle of attack of 4 degrees (Bansmer et al., 2018).

aircraft are far from benign. As illustrated in Fig. 1, ice can significantly alter the aerodynamic profile of a wing, leading to potentially hazardous flight scenarios.

The potential threat of icing that plagues airplanes is governed by a myriad of variables, such as the dimensions and density of particles, aircraft surface design, velocity of the aircraft, external temperature, and the temperature of the aircraft surface (Hann and Johansen, 2021).

Fig. 3. Typical mixed ice shape (Cao et al., 2018).

One significant influencer on the rate of droplet collection is the sizes and concentration of the particles (Banitalebi Dehkordi et al., 2013). For instance, smaller droplets tend to flow with the airstream, while their larger counterparts are more likely to collide directly with the wing. Additionally, the wing's leading edge curvature plays a pivotal role (Bowden et al., 1964; Cebeci and Kafyeke, 2003). Thin wings, due to their curvature, are more adept at capturing droplets compared to thicker wings. Another dynamic to consider is the aircraft's speed, as the frequency of droplet collisions surges in parallel with increasing airspeed. Summarizing the scenario, the most conducive environment for rapid droplet accumulation occurs when thin-winged aircraft are flying at elevated speeds through cloud environments rich in sizable droplets and a high liquid water content. Further examining the icing phenomenon, aircraft typically encounter three primary types of ice: rime (as shown in Fig. 2a), glaze (visualized in Fig. 2b), and a combination of the two, referred to as mixed ice (evident in Fig. 3) (Vukits, 2002). The definitions of each type of ice are detailed below:

Rime Ice: Originating from the freezing of minuscule supercooled water droplets upon hitting surfaces below freezing point (Buran, 2023), rime ice takes on a coarse, crystalline appearance, characterized by a mix of petite ice particles and entrapped air. The resultant ice layer obscures visibility and exhibits fragility due to its crystalline construct. The typical sites for rime ice formation include leading edges of aerofoils and engine inlets. Its presence can morph the aerodynamic characteristics of wings and disrupt the airflow into engines (Poots et al., 1776).

Glaze Ice: Unlike its rime counterpart, glaze ice emerges under conditions of marginally elevated temperatures (Addy et al., 1997). Environments rich in sizeable water droplets, abundant liquid water, and propelled by high air speeds delay the immediate freezing of water droplets upon wing contact. This delay propels these droplets to trail along the surface, freezing eventually unless displaced by wind currents. Glaze ice, owing to the compact arrangement of its droplets, is denser and exhibits a polished appearance. Its tendency to infiltrate the surface's pores prior to freezing lends it superior adhesive qualities. Often, its formation can be visually identified as single or dual horn-like protrusions (as depicted in Fig. 2b), a consequence of the air's flow direction (Papadakis et al., 2007). A study by Mikkelson (Mikkelsen et al., 1985) derived from five icing research flights ascertained that glaze ice critically hampers aircraft performance, a deduction not echoed as vehemently with rime or mixed ice. Additionally, Kind et al.'s (Kind et al., 1998) prolonged investigation into in-flight ice accretion simulation determined that the intricacies of glaze icing surpassed that of rime icing, challenging its computational modeling. In contrast, utilizing simplistic yet cogent mathematical models, Cao et al. (Cao and Hou, 2015; Cao and Huang, 2014; Cao et al., 2016) successfully illustrated ice accumulation on three-dimensional entities. While glaze ice's hallmark formation on the GLC-305 wing is a distinguishable double-horn shape,

its presence perturbs the wing's flow field, culminating in reduced lift, a diminished stall angle of attack, and augmented drag (Politovich, 2000).

Mixed Ice: The ever-fluctuating parameters of liquid water content and atmospheric water droplet sizes often result in ice formations exhibiting attributes of both rime and glaze ices. A specific note is that neither glaze nor rime ice can materialize at extreme cold temperatures of −6° and − 20 °C, respectively (Heinilä, 2021). Cloud systems within these temperature thresholds harbor a plethora of supercooled water droplet sizes. The resultant mixed ice encompasses the sleek, dual-horned characteristics of glaze ice, complemented by the milky translucence of rime ice, as portrayed in Fig. 3 (Papadakis et al., 2007).

The accumulation of ice on aircraft surfaces has been identified as a meteorological phenomenon that endangers aircraft flight safety (Piscitelli et al., 2023). The primary factors that affect the flight safety are as follows;

I. The degradation of the aerodynamic performance (e.g., reduction in the maximum lift coefficient and slope of the lift curve of the aircraft, and an increase in the drag and critical stall speed) of the aircraft (Piscitelli et al., 2023)
II. Pitch instability, which reduces the airfoil stall angle of attack and thereby makes it difficult for the aircraft to fly (Ignatyev et al., 2020)
III. Initiation of unexpected maneuvers (e.g., rolling and overturning as a result of the additional rolling moment generated by the formation of an ice ridge by droplets located beyond the ice protection device)
IV. The degradation of the control performance (e.g., an increase in the stick force because of the formation of tailplane ice could cause difficulties in maneuvering) (Muhammed and Virk, 2023)

Mitigating the risks of ice accumulation on vital aircraft surfaces necessitates the development of effective ice protection systems. A prominent solution in this regard is the adoption of ice-phobic coatings. Specifically crafted to obstruct the formation and adherence of ice, these coatings stand out in their efficacy. However, It is vital to draw a distinction between ice-phobicity and superhydrophobicity. The latter refers to a surface's capability to ward off water droplets, while the former is exclusively about resisting ice. Designed to inherently repel ice, ice-phobic surfaces play an invaluable role in scenarios where any ice formation is undesirable. The realization of such surfaces can be attributed to an array of techniques, including intricate surface modifications, specialized coatings, and advanced texturing. It is worth mentioning that while these ice-phobic surfaces might inherently repel water, their cardinal intent is the prevention of ice formation and its subsequent adherence.

In addition, ice protection systems, also known as anti-icing or deicing systems, are designed to either prevent ice formation or enable the aircraft to shed ice before it becomes problematic (Wang et al., 2021). The use of anti-icing coatings is a new method to reduce or prevent the accumulation of ice over equipment used in the aerospace and various other industries (Kulinich and Farzaneh, 2009; Kulinich and Farzaneh, 2011). An alternative, but equally attractive, method is the use of superhydrophobic surface (SHS) antifreeze coatings (Bascom et al., 1969). Although the concept of superhydrophobicity was first introduced by Ollivier (Ollivier, 1907) and then by Wenzel (Wenzel, 1936) and Cassie and Baxter (Cassie and Baxter, 1944) many years ago, it was not until Onda et al.'s publication (Onda et al., 1996) that a surge in articles on this topic began. In SHSs, air, which is a poor thermal conductor, is trapped in a layer under the surface to form a thermal barrier to delay ice formation, and the layer may even prevent ice from accumulating and adhering to the surface. The term "ice repellent" was coined to describe such surfaces. In order to control the movement and deflection of a water droplet and a liquid film (Nilsson and Rothstein, 2012), transport droplets without the use of external energy input (Khojasteh et al., 2020), and avoid or stimulate the development of tiny satellite droplets (Mertaniemi et al., 2011), the surface's wettability characteristics must be altered. Ueda and Levkin (Ueda and Levkin, 2013) revealed methods for creating hydrophilic-superhydrophobic designs that were previously published. These textured surfaces have been found to have several useful applications, including the precise control of droplet geometry and shape following impact, the separation of peptides with varying wettabilities, the management of bio-adhesion, the formation of high-density cell microarrays, and the isolation of different substances or cell types in separate spots on a single substrate. Song et al. (Song et al., 2015b) conducted an experimental study on droplet impact on a substrate consisting of SHS patterns (contact angle (CA) of 165°) on a hydrophilic glass slide (CA of 50°). During the impact on the hybrid surface (Mousavi and Lee, 2022; Mousavi and Roohi, 2023; Mousavi et al., 2022), they discovered that droplets can be split by a single stripe, and that the split time is independent of the impact velocity and is significantly shorter than the contact duration when only a totally SHS is utilized. Li et al. (Li et al., 2017a) investigated the migration of droplets over hydrophobic–hydrophilic hybrid surfaces that were textured with pillars and had hydrophobic side walls and hydrophilic tops, respectively. According to their findings, the migration process gradually increases as the droplet covers a larger area of more hydrophilic surface (HS).

Aviation safety is now exploring a new concept: the use of hybrid surfaces to prevent ice formation. This is the first time such an idea is being deeply considered. Hybrid surfaces, which have a combination of properties, differ from standard SHS or purely water-repelling surfaces. These hybrid surfaces have distinct water-resisting qualities that make them stand out and are believed to have great potential in various applications. However, there are still many unknowns about them. Detailed research is necessary to understand these hybrid surfaces better, especially how they can be adapted for different aircraft components and to determine the best water contact angle (CA) patterns. One main concern is understanding how these surfaces change the shape and duration of water droplets on them. Current research aims to understand how water droplets behave, especially when they hit these surfaces. Initial findings are promising; these surfaces might be effective in preventing ice build-up, especially on critical aircraft parts like wings. But like all new innovations, it will take thorough and patient research to truly understand their advantages and limitations for anti-icing. Our study begins by explaining the interaction of droplets with surfaces and the related theories. Later sections will discuss the behavior of water droplets on these hybrid surfaces, including their shape, how they break up, how they splash, and how long they stay on.

2. Research approach

In our pursuit to comprehensively understand the dynamics of hybrid surfaces in anti-icing, we embarked on a rigorous literature search, mining electronic databases for relevant insights. Our search strategy was anchored on pivotal keywords, including 'anti-icing,' 'SHSs,' 'hybrid surfaces,' and 'wettability gradient.' Our inclusion criteria were stringent, earmarking articles that delved into the interplay between contact angle and anti-icing efficacy. Additionally, we maintained an exclusive focus on English language publications that had been vetted through the peer-review process. Our initial search results were subjected to a meticulous screening protocol. We first weeded out duplicates, review articles, and those tangential to our primary research query. By meticulously examining the titles and abstracts, we filtered the pool further, ensuring relevance and potential for our study. Thereafter, we deep-dived into the full-text versions of these shortlisted articles, absorbing their methodologies, results, and discussions in detail. Our final phase involved a qualitative assessment, wherein we gauged the rigor, relevance, and research quality of the chosen articles, preparing us for a nuanced understanding and subsequent discussion on the topic at hand.

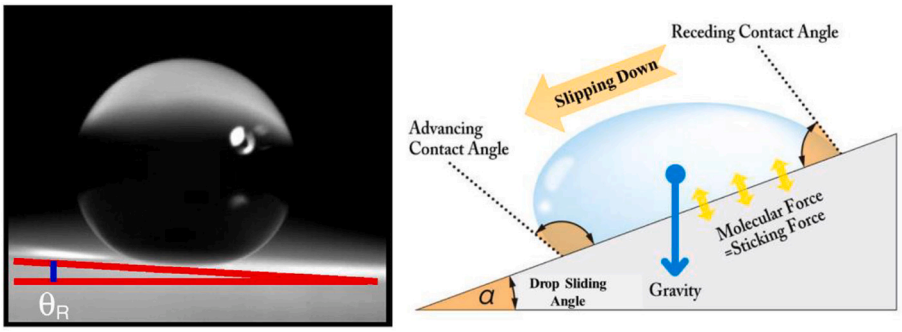

(a) (b)

Fig. 4. (a) Roll-off angle of a drop (Simpson et al., 2015), and (b) Schematic of droplet sliding angle (Nuraje et al., 2013)

3. Contact angles

The CA is pivotal in understanding a material's interaction with liquids. By observing these angles, we can deduce whether a fluid will form beads or cover a solid uniformly. Additionally, this knowledge lets us anticipate the liquid's form in varied structures, such as the curve it takes in a capillary (Decker et al., 1999). This angle is determined by placing a water droplet on a flat, planar, rigid, and uniform solid surface, as described by Butt (Butt et al., 2003). Due to the non-diffusive nature of the liquid, the droplet maintains a constant shape and reaches an equilibrium contact angle that reflects the surface wettability (Butt et al., 2003). Geometrically, the CA is measured at the interface of the liquid-solid-gas phases, as stated by Elbahri et al. (Elbahri et al., 2007). A surface with a CA below 90° is considered hydrophilic, while a surface with a CA exceeding 150° is regarded as SHS, according to Chieng et al. (Chieng et al., 2019). In addition, it is worth noting that an extremely high water CA of nearly 180° was fabricated via coating a substrate using soot (Ollivier, 1907).

3.1. Hysteresis CA

The difference between the advancing and receding CAs (Göhl et al., 2018; Good, 1952) is referred to as hysteresis CA, and it has been the subject of several studies. The unevenness of a rough solid surface is effective in giving rise to hysteresis, and therefore, it should be investigated (Luo et al., 2017; Xing et al., 2020; Xu, 2016; Xu et al., 2017). Hysteresis may occur because of changes in the solid surface energy resulting from liquid absorption (i.e., a smaller receding CA is obtained) (Hall, 1966). In the equation that describes surface hydrophobicity, the hysteresis is greater than the maximum CA. In general, as evident in Eq. (1), the force required to initiate a droplet movement on a surface is directly proportional to the hysteresis CA (Dussan and Chow, 1983).

$$F = \gamma_{LV}(cos\theta_R - cos\theta_A) \quad (1)$$

where F is the critical line force per unit length of the drop perimeter. Also, γ_{lv} is the liquid surface tension, θ_R and θ_A are the receding and advancing contact angles, respectively. Recently, a new model for determining the CA hysteresis of an SHS was presented by Zhu and Dai (Zhu and Dai, 2019).

3.2. Roll-off and sliding angles

The roll-off angle of a SHS, as shown in Fig. 4a, is a critical parameter that indicates the degree of surface hydrophobicity(Simpson et al., 2015). The roll-off angle, which is typically measured by gradually tilting the surface until a water droplet begins to slide or roll off, is a direct reflection of the interplay between surface tension, gravity, and the adhesion forces between the droplet and the surface. As shown in Fig. 4b, the threshold angle at which a droplet starts to slide on the surface is known as the "drop sliding angle" (α) (Pierce et al., 2008). The roll-off angle of SHSs is typically lower than 5°, indicating their excellent water-repelling properties (Carré and Mittal, 2009). However, high-quality SHSs can achieve even lower roll-off angles, potentially lower than 1°, which highlights the importance of careful fabrication and surface engineering techniques. The roll-off angle is an essential factor in many applications, such as self-cleaning coatings, anti-icing surfaces, and microfluidic devices, where precise control over surface wettability is crucial for effective performance (Mittal, 2014).

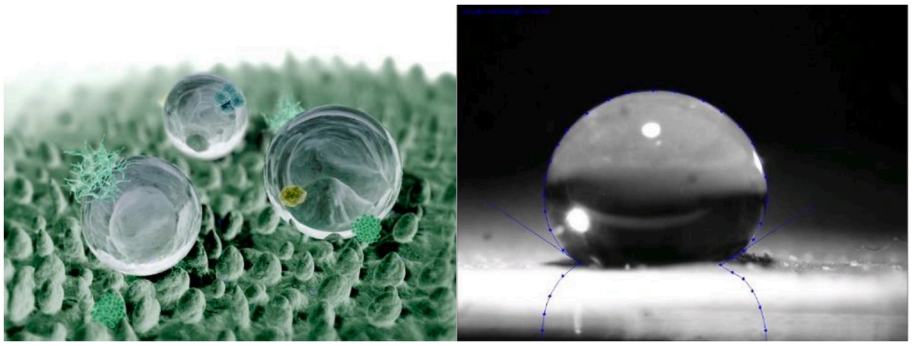

(a) (b)

Fig. 5. a) Computer graphic images of (a) a lotus leaf surface (bump diameter: 11 μm) (Ivanović et al., 2018) and (b) a water drop on a lotus surface indicating a CA of about 146°–147° (Zhang et al., 2016).

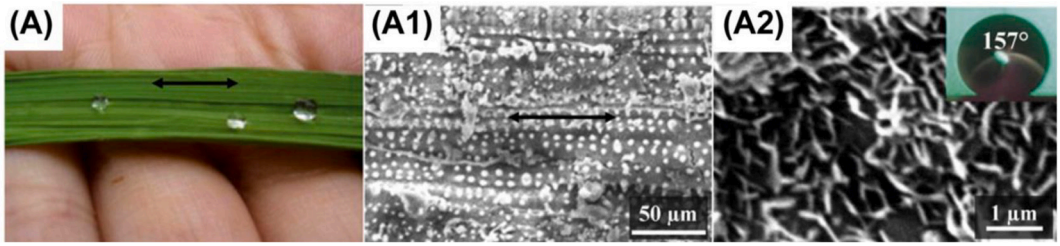

Fig. 6. Rice leaf structure at different micro-lengths (Crawford and Ivanova, 2015).

Table 1
Examples of other plants with SHS features.

CA,°	plants
150	*Cladium mariscus*(Neinhuis and Barthlott, 1997)
159	*Canna glauca*, *Cleome arborea*(Neinhuis and Barthlott, 1997)
160	*Eryngium bourgatii* and *Belamcanda chinensis* (Neinhuis and Barthlott, 1997)
161	*Leymus Arenarius* Leaves, *Macleaya Cordata*, And *Elymus Arenarius* (Koch and Barthlott, 1893 Neinhuis and Barthlott, 1997)
162	Perfoliate Knotweed (Wolfs et al., 2013)
164	Taro Plant Leaves (Koch and Barthlott, 1893)
167	Purple Setcreasea (Wolfs et al., 2013)

4. Natural SHSs

4.1. Plants

There are many examples of SHSs that occur naturally, and they include the surface of plants and insects (Bhushan and Jung, 2011; Byun et al., 2009; Wendell et al., 2006). The existence of a runoff surface dates back thousands of years (Barthlott et al., 2016). On the basis of observations, there are about 24,000 different plant and animal species that have an SHS part that is surrounded by a crystalline waxy layer. This layer is usually composed of 20–30long-chain hydrocarbons, including alkanes, aldehydes, ketones, fatty acids, alcohols, and esters (Barthlott et al., 2016). As stated, bumps at the micro- and nanoscale are responsible for the hydrophobicity (see Fig. 5a). One of the best-known examples of this structure is the lotus leaf, with a CA approaching 146°–147° (see Fig. 5b). Scanning probe microscopy observations have shown that the leaves are coated with 1–5 μm lumps known as papillae, which are located beneath a waxy crystalline top layer.

Fig. 6 depicts rice leaves as another natural SHS, and similar to the lotus leaf, they are covered with hierarchical structures. Yet, the arrangement of the micro-Nano hierarchical structure on the rice leaves is anisotropic (quasi–1D order parallel to the leaf edge). The surface pattern includes sinusoidal grooves, which are covered by micro-papillae containing wax Nano-bumps (Feng et al., 2002). Therefore, the hierarchical structure enhances the self-cleaning (SC) capability of the rice leaf (Nishimoto and Bhushan, 2013).

Table 1 shows some instances of the plants with SHS characteristics. Evidently, the range of CA is varied which is due to the surface properties of the plants.

The aroid water lettuce *Pistia* and the floating fern *Salvinia* are other plants with HSs with unique features. These surfaces do not have micro−/nanostructured bumps, and they typically have hairy surfaces. Epicuticular waxes of plants are only 2D wax films (Kaul, 1976; Neinhuis and Barthlott, 1997). Large filiform multicellular trichomes cover the surface of *Pistia*. However, *Salvinia*'s surface is covered with various types of multicellular trichomes, and they include single, two, and four hairs in *S. cucullata* (identical to those in *Pistia*), *S. oblongifolia*, and the *S. auriculata* complex, respectively.

Salvinia (Barthlott et al., 1994) conducted initial scanning electron microscope examinations (see Fig. 7a and b) that revealed that such plants have rodlet-shaped thin waxes vertical to the surface. Rodlets have been detected on trichomes and leaf surfaces. In the genus *Salvinia*, epicuticular waxes vary slightly; however, the leaf size and leaf shape, as well as trichomes, differ between species. Trichomes in *Salvinia* can be classified into four types: single (*S. cucullata* and *S. hastata*), double (*S. oblongifolia*), quadruple (*S. natans* and *S. minima*), and quadruple joined (*S. auriculata*, *S. biloba*, *S. herzogii*, and *S. molesta*) trichomes. The trichome length ranges between 200 μm (*S. oblongifolia*) and 800 μm (*S. minima*), and it is almost consistent with the leaf size for various species (varying from 5 mm (*S. minima*) to 51 mm (*S. oblongifolia*)). Despite their different shapes, all trichomes and their epicuticular waxes contribute to the superhydrophobicity of *Salvinia* (Cerman et al., 2009).

Fig. 7. (a) Droplet on a *S. oblongifolia* leaf; the air trapped between trichomes is responsible for the silvery shine, which is a reflection of the lower surface of the drop (Cerman et al., 2009). (b) The *S. molesta* fern has an extraordinarily complex surface (i.e., it can survive underwater).

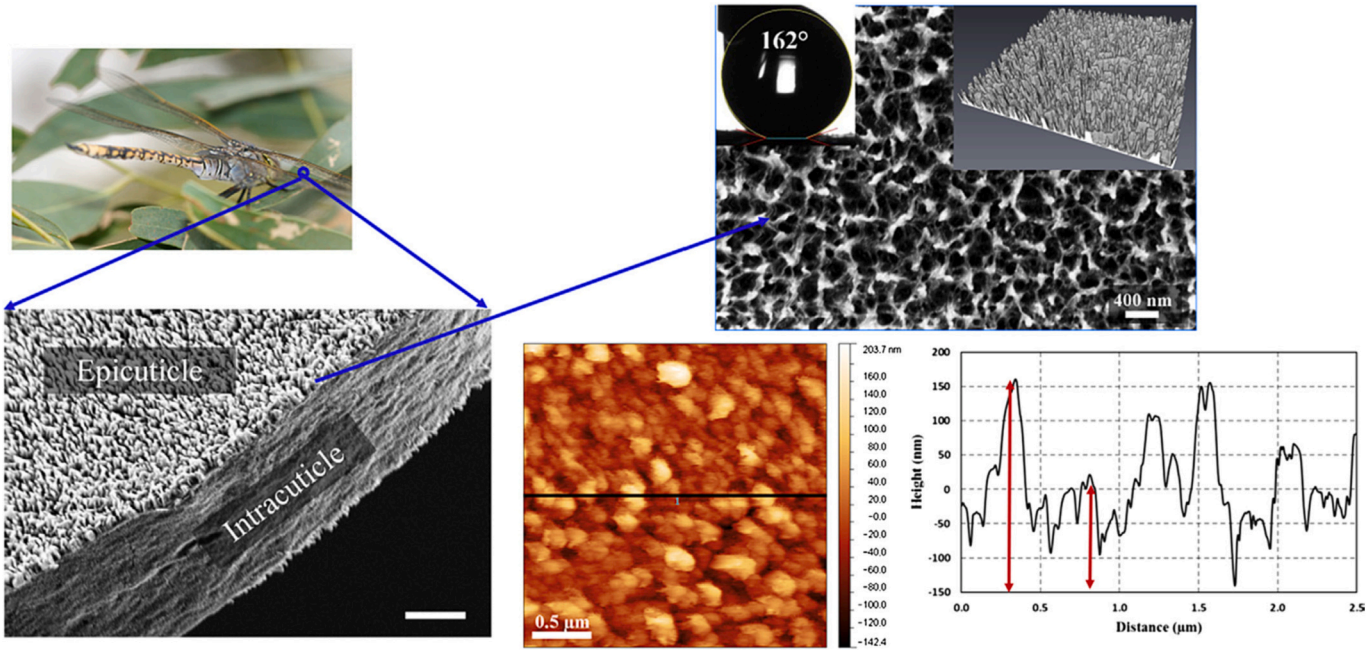

Fig. 8. Wettability of the dragonfly *Hemianax papuensis's* wing (Crawford and Ivanova, 2015).

On the basis of the latest tests on various species of *Salvinia* and given their capability to maintain air films underwater, the species with the largest leaves, namely *S. oblongifolia*, is known to stay dry underwater most viably (Cerman et al., 2009). Furthermore, submerged *S. oblongifolia* leaves have been found to retain an air film for up to seventeen days. By contrast, other examined species, such as *S. molesta*, *S. biloba*, *S. minima*, and *S. cucullata*, remain dry only for four to five days. Because these tests have been done with plant leaves that were alive, it cannot be said that the air film's longevity resulted from physiological processes such as photosynthesis (Cerman et al., 2009).

4.2. Insects

Insect wings are one of the most well-known HSs since a complex structure on their surface imparts antifogging and wetting characteristics to the surface. During the past decade, insects such as butterflies (Darmanin and Guittard, 2015), cicada (Darmanin and Guittard, 2015), water strider (Bush et al., 2007), dragonfly (Schroeder et al., 2018), and damselfly (Truong et al., 2017) have been found to show antifogging/wetting behavior (Cheeseman et al., 2018; Feng et al., 2007).

The outer layer of an insect wing (cuticle) serves as a block and it interacts with the environment. This layer is covered by a single layer of epidermal cells, and it has a lipophilic structure (Pavković-Lučić et al., 2012; Samuels et al., 2008). Furthermore, the epicuticle, being the cuticle's outermost layer, is a combination of aliphatic hydrocarbons and their derivative mixtures. Such mixtures contain one or more oxygen functional groups (Koch and Ensikat, 2008; Samuels et al., 2008). The intracuticular layer is located under the epicuticular compounds of chitin and protein (Lockey, 1988). These components are self-organized in the cuticle's epicuticular layer, and they form a smooth 2D wax film or even a 3D wax crystal structure. Furthermore, such structures help organisms adapt to their surrounding conditions. As shown in Fig. 8, an array of nanopillars covering the dragonfly *Hemianax papuensis*'s wing surface maintains an air volume during the contact of the wings with liquids. In particular, the CA of the *H. papuensis*'s wing surface is about 161°. Furthermore, low hysteresis and sliding CAs of <10° show the SC ability of the wing surfaces (Ivanova et al., 2013b). These insects' SC characteristics are more sensitive to turbulent flying conditions (Nishimoto and Bhushan, 2013). The morphological characteristics of insect wing surfaces were classified in terms of setae (high aspect ratio needles or hairs), denticles (tooth-like projections), fractals (disorderly array of fine nanoscale protrusions), and layered cuticles (surfaces with overlapping scale-type structures) by Byun et al. (Byun et al., 2009). It should be noted that the presence of fractals, denticles, and layered cuticles is associated with the formation of SHSs. However, the state term "on the surface" means that the surface is not SH. References (Byun et al., 2009; Watson et al., 2010) summarized the CA of some species on the basis of their structural morphologies.

Table 2
Some examples of the insects with SHS characteristics.

CA, °	Insects
156	*Grocus bore* (CA = 159°) (Byun et al., 2009)
159	*Tabanus chrysurus* (CA = 156°) (Byun et al., 2009)
160	*Pantala flavescens* (CA = 160°) (Byun et al., 2009)
162	*Artogeia canidia* (CA = 162°) (Byun et al., 2009)
165	*Meimuna opalifera* and Homoptera (CA = 165°) (Wolfs et al., 2013)
167.6	water striders (CA = 167.6°) (Gao and Jiang, 2004)

The wing surface of *Meimuna opalifera* (Walker) cicada is covered with a dense nanopillar layer, which can entrap air (Tripathy et al., 2017). Furthermore, it has been shown that the topographic hierarchy of a surface has a major role in imparting surface superhydrophobicity. However, other factors should be considered. According to the Cassie–Baxter theory, the surface materials' chemical properties and their ability to entrap air are the two main factors that should be considered for examining the surface hydrophobicity. Specifically, air entrapment is related to the roughness and topology of the surface (Quetzeri-Santiago et al., 2019). Owing to the density, size, and shape of the hierarchical roughness, the hierarchical surface can entrap air (Langley et al., 2018). The features of superhydrophobicity and SC of insect wings help the insects to keep the wings free from contaminants. Therefore, these characteristics help insects to retain their anti-reflective characteristics. It is also noteworthy that the wings of some insects such as dragonfly are antibacterial (Ivanova et al., 2013a; Ivanova et al., 2012). It is speculated that these characteristics are directly related to the surface wettability (Pogodin et al., 2013). Table 2 indicates some example of insects with SHS features.

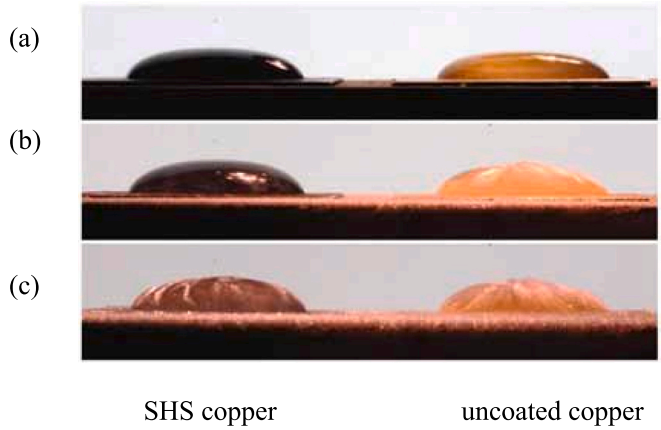

Fig. 9. Ice formation by water droplets on the two surfaces at −7 °C. a- the drops were just deposited; their colors reflect the substrates. b- the drop on flat copper has frozen. C- both drops are frozen (Tourkine et al., 2009).

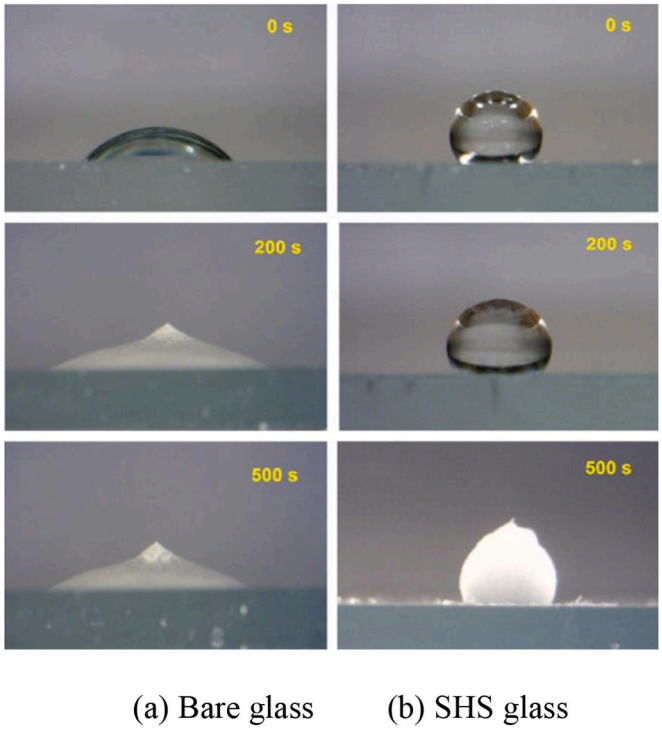

Fig. 10. Icing process of a water droplet on (a) the bare glass and (b) SHS glass (CA = 153°) (Ahmad and Eshaghi, 2018).

5. Applications of SHSs

Importantly, the industrial applications of HSs cover an extremely wide range and include SC surfaces (Hu et al., 2018; Kang and Li, 2017), anti-smudging surfaces (Kim and Lee, 2019), anti-sticking surfaces (Kim and Lee, 2019), water harvesting (Gao et al., 2018), heat transfer enhancement (Betz et al., 2013), medical and electrical microstructures (Dietz et al., 2010), drag reduction (Nouri et al., 2013), antifogging surfaces (Lomga et al., 2017), smart fabric synthesis (Li et al., 2017b), corrosion reduction in marine environments (Dou et al., 2018), waterproof textiles (Barberoglou et al., 2009), solar energy panels (Barthlott and Neinhuis, 1997), low-friction coatings (Qiu et al., 2013), and separation of water and oil (Sotoudeh et al., 2023). Further, the application of hydrophobic coatings in the aerospace industry can be divided into four categories: (1) anti-icing; (2) drag reduction; (3) SC; (4); and corrosion resistance (Brown et al., 2020). Additionally, hydrophilic and SHS coatings can be used in the construction industry to enhance the durability and quality of building materials. Specifically, HSs can be used in the textile (SC fabrics), automotive and aerospace (SC glass, car bodies, and nonadhesive surfaces), and optical industries (cameras, sensors, lenses, and telescopes). In addition, in recent years, research has been conducted on reducing ice adhesion and delaying the formation of ice SHSs (Chu et al., 2019a; Chu et al., 2018; Guo et al., 2012; Yang et al., 2020). In this section, studies on these subjects are reviewed.

Due to bubbles form, Chu et al. (Chu et al., 2019b) found that the final ice droplet is not a solid piece of ice but rather a porous medium. Tourkine et al. (Tourkine et al., 2009) performed an experiment to determine the possibility of superhydrophobicity delaying the static formation of ice. An uncoated copper plate and an SHS copper plate were used, and the forward and backward CAs were 165° and 155°, respectively. Fig. 9 shows a comparison between two drops of water deposited on the SHS and on the uncoated copper plate. On both surfaces, a thin circular groove with a radius of 10 nm was used to fix the contact line and to allow the droplet volume to change without any change in the contact surface. This allowed the researchers to determine the effect of the surface structure on the icing process. The first-row images of Fig. 9 were recorded immediately after deposition. When the second-row images were recorded, the droplet was observed to be on the SHS surface without the formation of ice. In contrast, the droplet on the uncoated surface was beginning to freeze. The droplets on the left image had frozen when the last-row images were obtained.

In the work by Ahmad and Eshaghi (Ahmad and Eshaghi, 2018), water droplets were placed on an SHS-coated glass and on bare glass, and the icing was examined in order to determine whether icing occurred. The temperature within the chamber was maintained at $12°C$ at all times. Fig. 10 depicts water droplets and ice formation on the two surfaces. The water droplet on the modified film had a smaller contact surface area and a larger CA than that on the bare glass sample, whereas the water droplet on the bare glass sample had a larger contact surface area and a smaller CA. As shown in Fig. 10, droplets on the bare glass took around 200 s to completely freeze, whereas those on a highly water-repellent surface required 500 s to completely freeze. Temperature-dependent reductions in the values of the water CA on bare glass and clear SHS glass were seen when the surface temperature was decreased. Water molecules were attracted to cold surfaces, and they were adsorbed on the surfaces. These findings showed that the delay in ice formation was greater on the SHS film surface due to the reduced contact area between the film and water (Lengaigne et al., 2020; Memon et al., 2023; Piscitelli et al., 2023). This limited contact is associated with the air that becomes trapped beneath the water droplets, serving as a thermal barrier. This not only postpones the freezing process but also hinders ice accumulation and its adhesion to the hydrophobic surface. Additionally, the interlocking effect of ice on rough surfaces plays a significant role in these interactions, as described in a study by Yin et al. (Yin et al., 2011). Classical nucleation theory (Kalikmanov, 2013) and the heat transfer between the droplets and the SHS suggest that the difference in the surface wettability at surface temperatures $<0°C$ was responsible for the difference in the solidification time (Jin et al., 2016). The results of icing tests revealed that the time necessary for the entire icing process, as well as the time required to initiate icing, on the SHS was much longer than the time required for the bare glass surface. Thus, the improved film could reduce the amount of ice formed on the glass surface.

Fig. 11 compares the continuous growth of ice on aluminum samples with different CAs when the aluminum samples were sprayed with supercooled water droplets in a wind tunnel at an operating temperature of −6 °C and a wind speed of about 3 m/s (Wang et al., 2010a). The figure depicts the ice accumulation on several metal surfaces with different compositions. When the SHS material was originally tested, only a few regions around the boundaries of the sample were covered by individual water droplets, as evident in Fig. 11a. Increasing the spraying

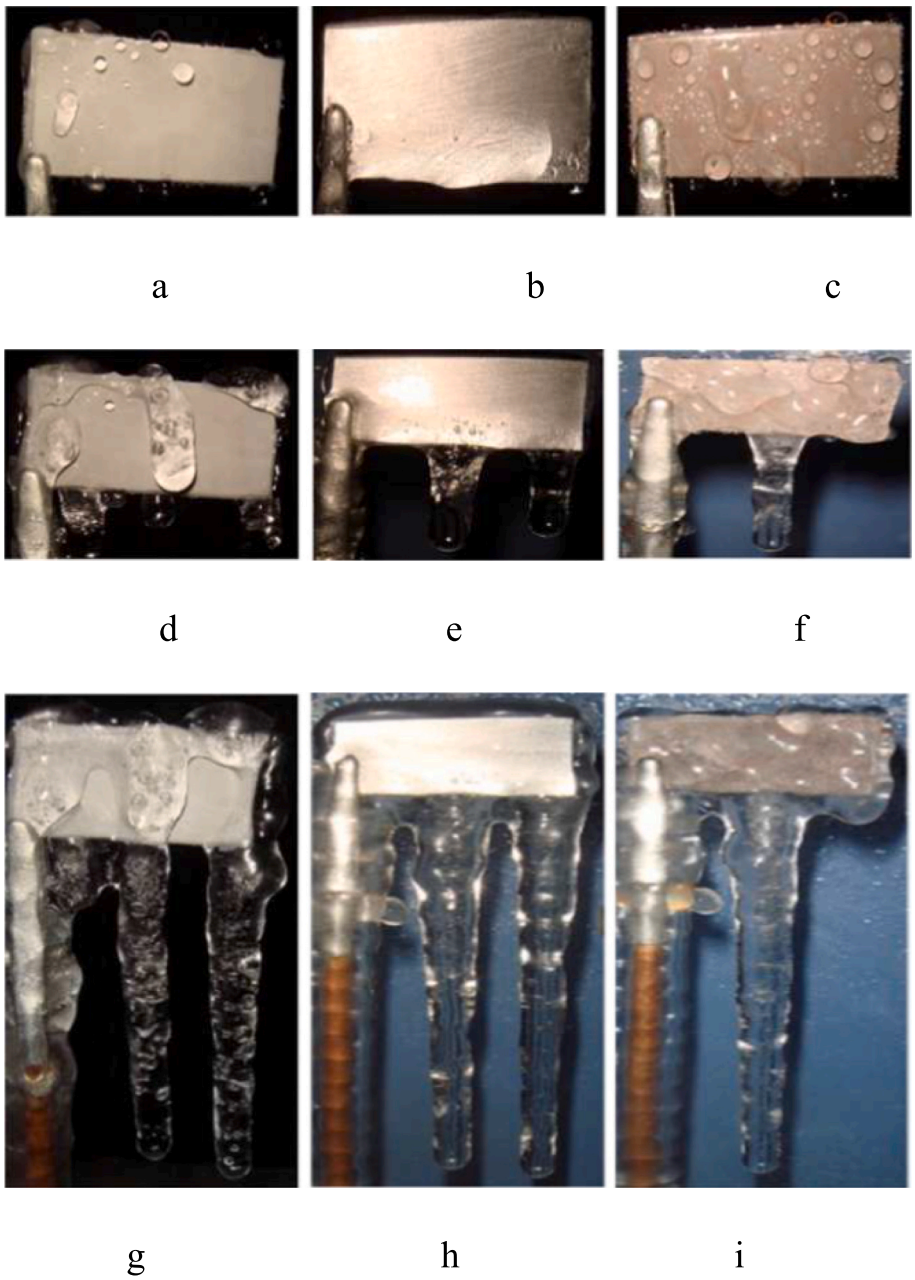

Fig. 11. Ice accretion on different aluminum sheets: after 1 min on the (a) SHS, (b) HS, and (c) surface coated with room-temperature-vulcanized silicone rubber; after 10 min on the (d) SHS, (e) HS, and (f) silicone-rubber-coated surface; and after 30 min on the (g) SHS, (h) HS, and (i) silicone-rubber-coated surface (Wang et al., 2010a).

time resulted in the rapid transformation of water droplets on the surface into ice, and the other water droplets showed a tendency to move close to the initially formed ice crystals as the spraying duration increased. Finally, some icicles began to grow on the surface of the water. Notably, no new ice crystals grew on the anti-icing region, as shown in Fig. 11d and g, even after 10 to 30min of spraying, indicating that the anti-icing solution was effective. When supercooled water was sprayed on the hydrophilic sample, a water film developed in <10 s and quickly solidified into a full coating of ice (see Fig. 11b). As shown in Fig. 11e and f, the thickness of the coating of ice and the length of the icicles grew as the spraying duration increased (Fig. 11h). Separate water droplets covered the aluminum sample coated with room-temperature-vulcanized silicone rubber within a minute of water being sprayed on the sample. It can be clearly observed in Fig. 11f that a complete ice layer emerged only after a total of 10 min of spraying. Nevertheless, once a layer of ice developed on the silicone-rubber-coated aluminum surface, the ice- repellent performance of the silicone rubber coating dropped significantly. Alterations in the ice coating and icicles observed with simple aluminum were identical to those observed with titanium dioxide (Laroche et al., 2021). Compared with the hydrophilic coating, an SHS coating provided to the aluminum surface could significantly reduce ice accretion on the aluminum surface.

Fig. 12 displays the ice accumulation tests on supercooled Nanocoatings and microstructures on which supercooled water droplets were allowed to fall from a height of 100 mm. Three different tilt angles were used (0, 30°, and 60°) (Mishchenko et al., 2010). In the three cases, the substrate temperature was −10 °C and the tilt angle was 30°. Micrographs of example SHSs are shown in the insets, and they include posts, bricks, blades, and honeycombs (scale bars: 10 μm). The authors

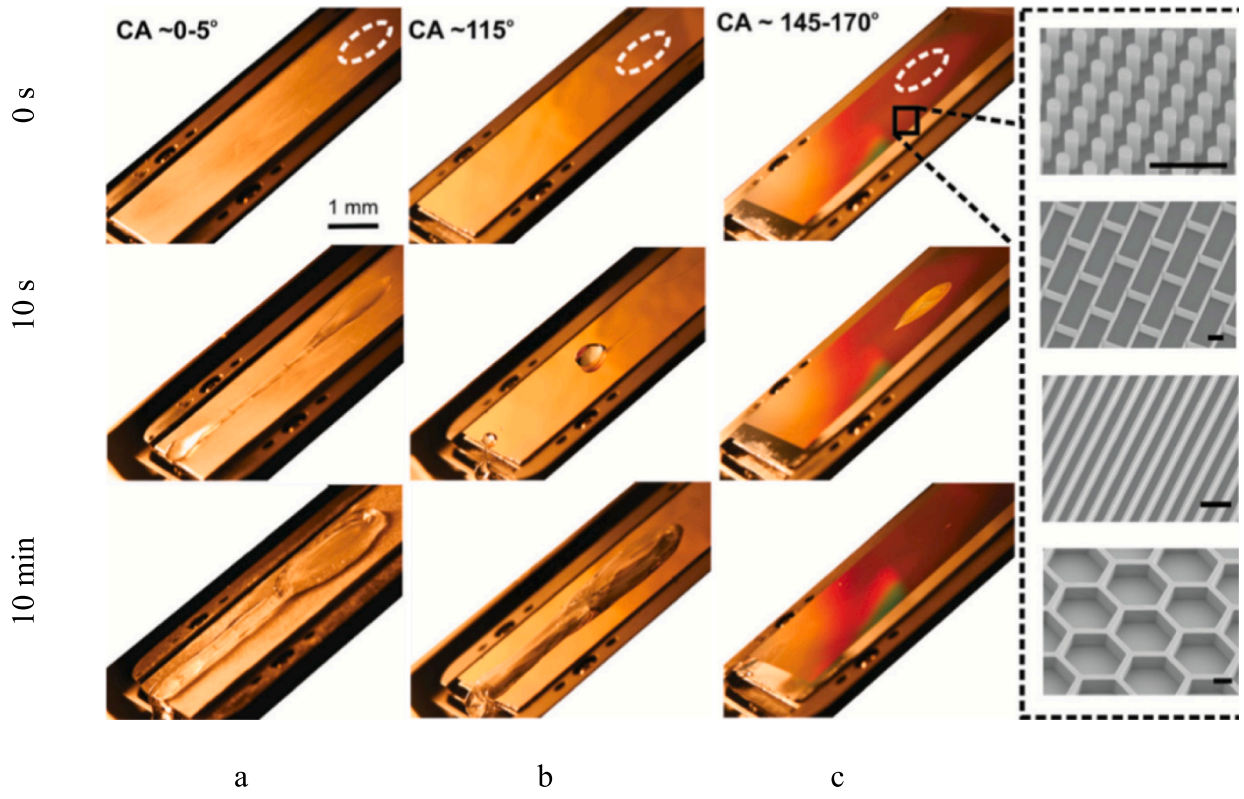

Fig. 12. Ice accumulation on (a) flat aluminum (hydrophilic), (b) smooth fluorinated silicon (hydrophobic), and (c) microstructured fluorinated Si (SHS) (Mishchenko et al., 2010).

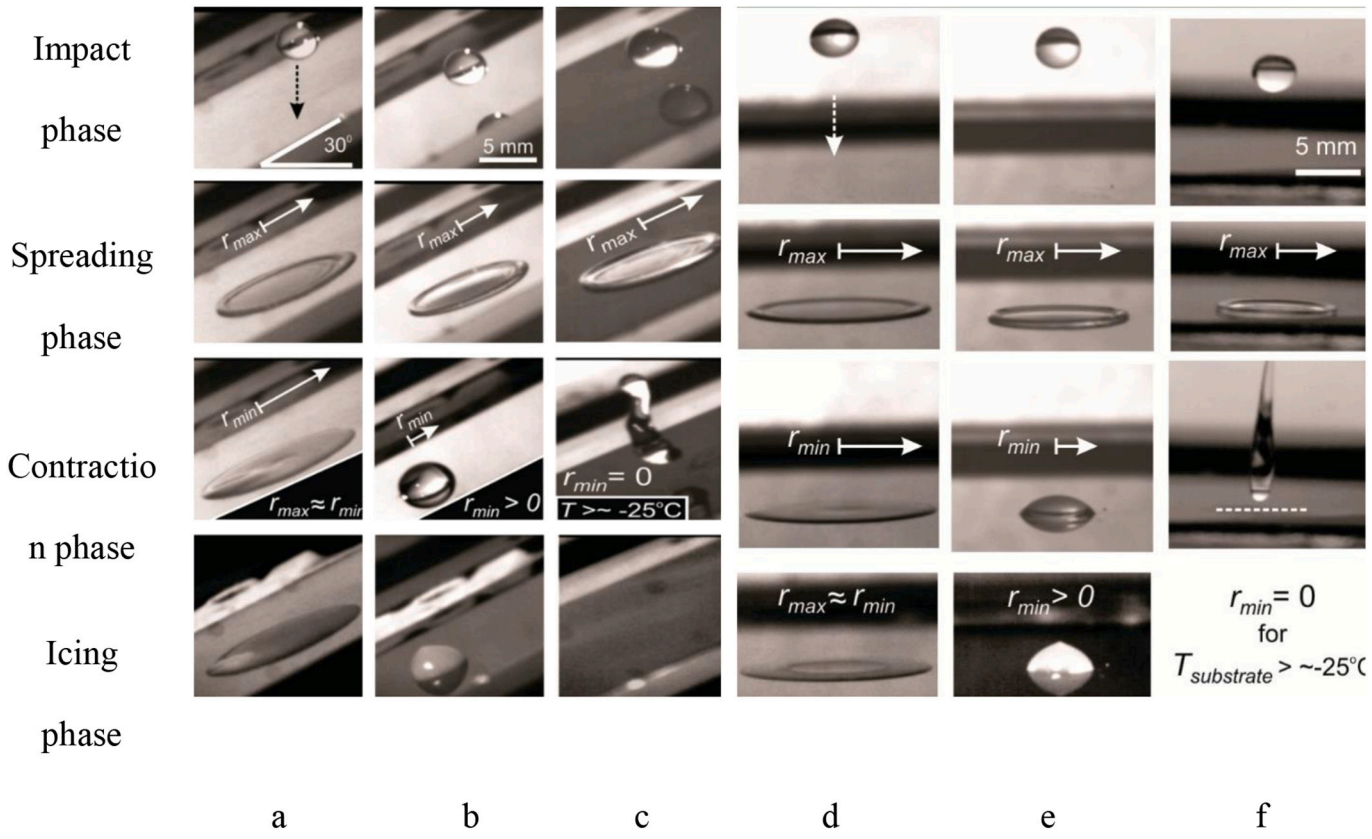

Fig. 13. Dynamic behavior of droplets impacting on 30° tilted surfaces of (a and d) flat aluminum (HS), (b and e) smooth fluorinated Si (HS), and (c and f) microstructured fluorinated Si (SHS) after falling from a height of 10 cm at a substrate temperature below 0 °C (Mishchenko et al., 2010).

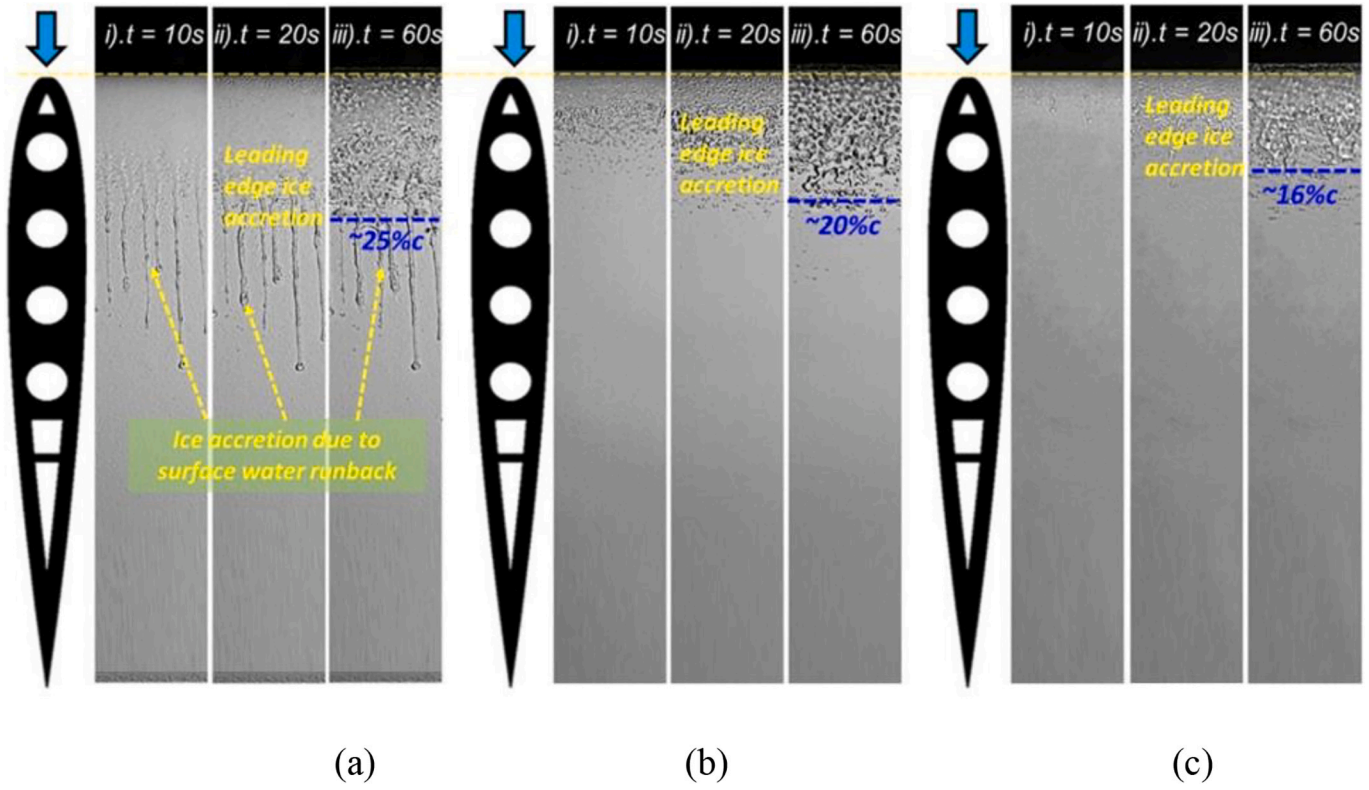

Fig. 14. Dynamic ice formation mechanisms on (a) enamel-coated, (b) SHS-coated, and (c) polytetrafluoroethylene- coated airfoil models before the immersion of the airfoil models in deicing fluids (Zhang et al., 2021).

found that the delay in ice formation on the flat hydrophobic surface relative to the HS was about one minute, but after 10 min, both substrates showed significant ice accumulation (see Fig. 12). On the other hand, the SHS remained virtually ice-free for 10 min after the test. Ice repellency was examined for many different geometries, tilt angles, and droplet and substrate temperatures.

The images in Fig. 13 demonstrate the behavior of 15 μL droplets when they hit a 30° tilted and horizontal surface at a temperature below 0 °C after falling from a height of 10 cm. The images from top to bottom show the droplet impact, maximum spreading (r_{max}), maximum retraction (r_{min}), and freezing. On HSs (aluminum) and hydrophobic Si surfaces, the droplets did not retract completely after spreading ($r_{min} > 0$), stayed in contact with the substrates, and froze in a few seconds for substrate temperatures below −10 °C. By contrast, on the SHS, they fully retracted and bounced off the surface without leaving any residue at substrate temperatures lower than $-25\,^{\circ}C$ to $-30\,^{\circ}C$ (Mishchenko et al., 2010).

Fig. 14 depicts the dynamic processes of ice accumulation on the surface of an airfoil/wing model covered with SHS coatings (i.e., a SHS and polytetrafluoroethylene) before being immersed in deicing solutions (Zhang et al., 2021). Ice collection on an airfoil/wing model covered with a hydrophilic enamel coating is shown in this figure as an example of the effectiveness of an SHS coating for aircraft for in-flight icing reduction. Based on the finding by Zhang et al. (Zhang et al., 2021), ice accumulation on the surface of the airfoil model was rapid when supercooled water droplets transported by a frozen-cold airflow impacted the airfoil model's surface. Additionally, the ice adhesion strength on the polytetrafluoroethylene surface is considerably lower at 20 kPa ± 5 Kpa compared to the SHSs, which have a strength of 105 kPa ± 10 Kpa (Zhang et al., 2021). As a result, the protection of the ice layer accreted near the airfoil's leading edge on the polytetrafluoroethylene-coated airfoil surface was observed to be noticeably less than that on the SHS-coated airfoil surface. After 60 s of ice accumulation, it was observed that the ice layer on the airfoil's front surface grew at a downstream position of X/C = 20% on the SHS-coated airfoil model. An equivalent ice layer was formed at X/C = 16% on the polytetrafluoroethylene-coated airfoil model. However, the ice layer coverage over the airfoil's front surface extended downstream to X/C = 25% on the hydrophilic-enamel-coated airfoil surface.

As mentioned by Liu and Hu (Liu and Hu, 2018) investigated the unsteady heat transfer and dynamic ice accretion process over an airfoil/wing surface under different icing conditions through experiments and developed a theoretical model to evaluate the convective heat transfer coefficient. The study used a high-speed infrared thermal imaging system to capture surface temperature measurements and quantitatively characterized the transient behaviors of droplets impingement, surface water runback, and dynamic phase changing processes. The study also determined the water collection efficiency distribution around the airfoil surface and incorporated it into the theoretical heat transfer model to estimate the convective heat transfer coefficients. The study found that insufficient heat transfer caused only a fraction of the impacting supercooled water droplets to instantly freeze to ice under wet glaze, while the remainder accumulated as liquid on the airfoil's front surface. The unfrozen surface water ran back down the airfoil, giving rise to several water rivulets that flowed along the airfoil's downstream surface. This moved the surface water away from the airfoil's leading edge (Zhang et al., 2015). Partly because of the fact that the ambient airflow temperature was adjusted to be noticeably less than the frozen temperature of the water, it was found that the runback surface water was frozen into ice, eventually forming rivulet-shaped ice formations further downstream, as shown in Fig. 14a. Additionally, it was revealed that after covering the airfoil/wing models with SHS coatings, the quantity of ice accretion over the SHS airfoil surface of the test model was reduced compared with the hydrophilic airfoil surface. The SHS coated airfoil surface had less ice layer coverage at its leading edge (i.e., because of the direct impingement of the supercooled water

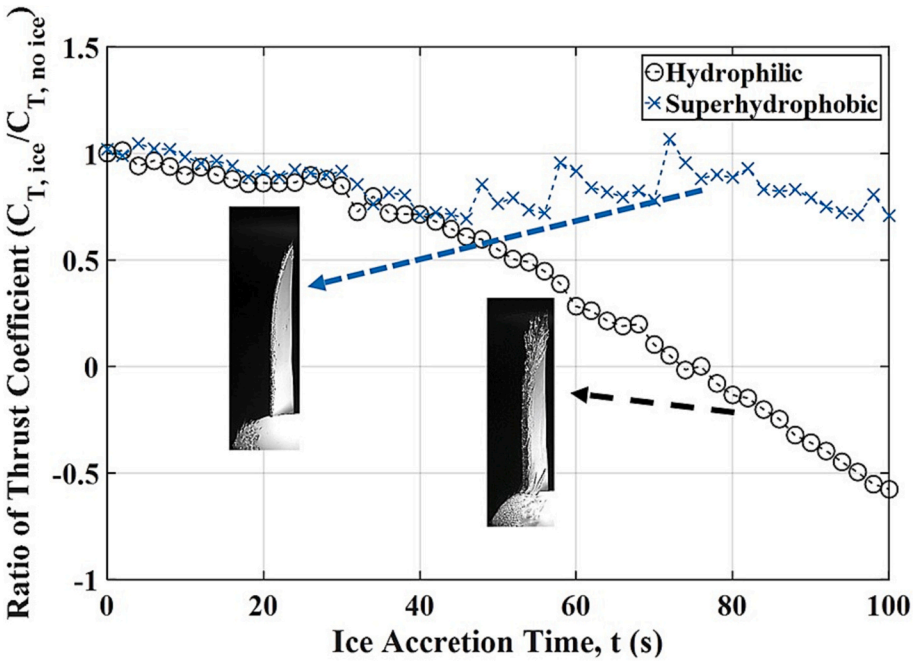

Fig. 15. Measured propeller model thrust for various surface wettabilities (Liu et al., 2018).

droplets), and there was no evidence of water runback or rivulet-shaped ice structures on its surface. A side-by-side analysis of the ice formation images in Fig. 14 indicates that SHS coatings can be highly effective for icing prevention on aircraft. According to Zhang et al. (Zhang et al., 2021c), the significantly reduced quantity of ice accumulation on an SHS and on polytetrafluoroethylene-coated airfoil surfaces is mainly because of two factors. First, it is expected that the hydrophobic coatings, SHS, and polytetrafluoroethylene surfaces would be considerably more slippery than the hydrophobic coatings-SHS, allowing impacting supercooled water droplets to bounce off and/or roll away from the airfoil surfaces before freezing into ice. Additionally, because an SHS substantially reduces the ice adhesion strength, the incoming airflow's aerodynamic shear forces would more swiftly sweep away the accreted ice forms from the surface of the airfoil.

Mora et al. (Mora et al., 2020) studied the ice accumulation and stickiness characteristics of two types of Quasicrystals coatings, made of Al, Fe, Cu, and Cr, and designed to prevent sticking. They measured the wetting properties, hardness, roughness, ice accumulation behavior, and ice stickiness of the coatings and compared them to other materials such as polytetrafluoroethylene and two paints with and without ice-resistant properties. The results showed that polytetrafluoroethylene had the lowest ice stickiness and Quasicrystals-1 had similar ice accumulation

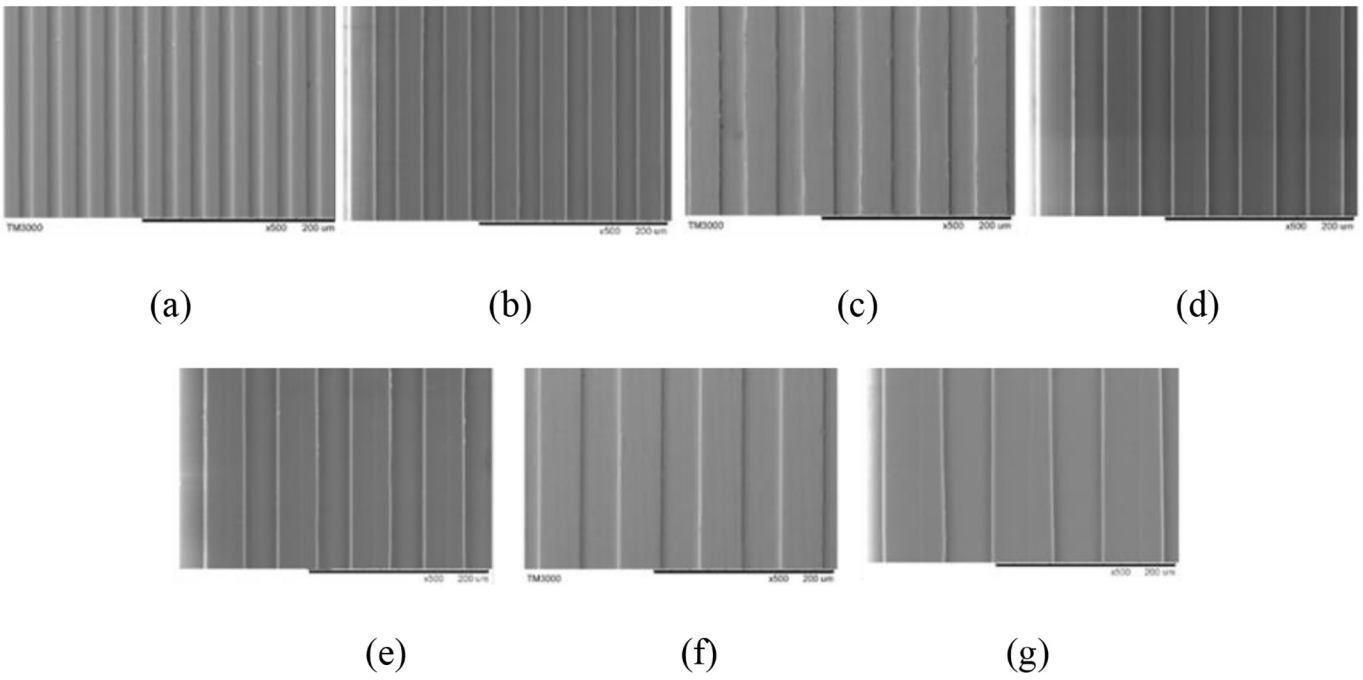

Fig. 16. Scanning electron microscope and 3D profiles of micro-grooves fabricated on cyclic olefin copolymer samples with different groove widths and spacing: (a) 15, (b) 25, (c) 30, (d) 35 m, (e) 40, (f) 45, and (g) 60-μm (Cheng et al., 2020).

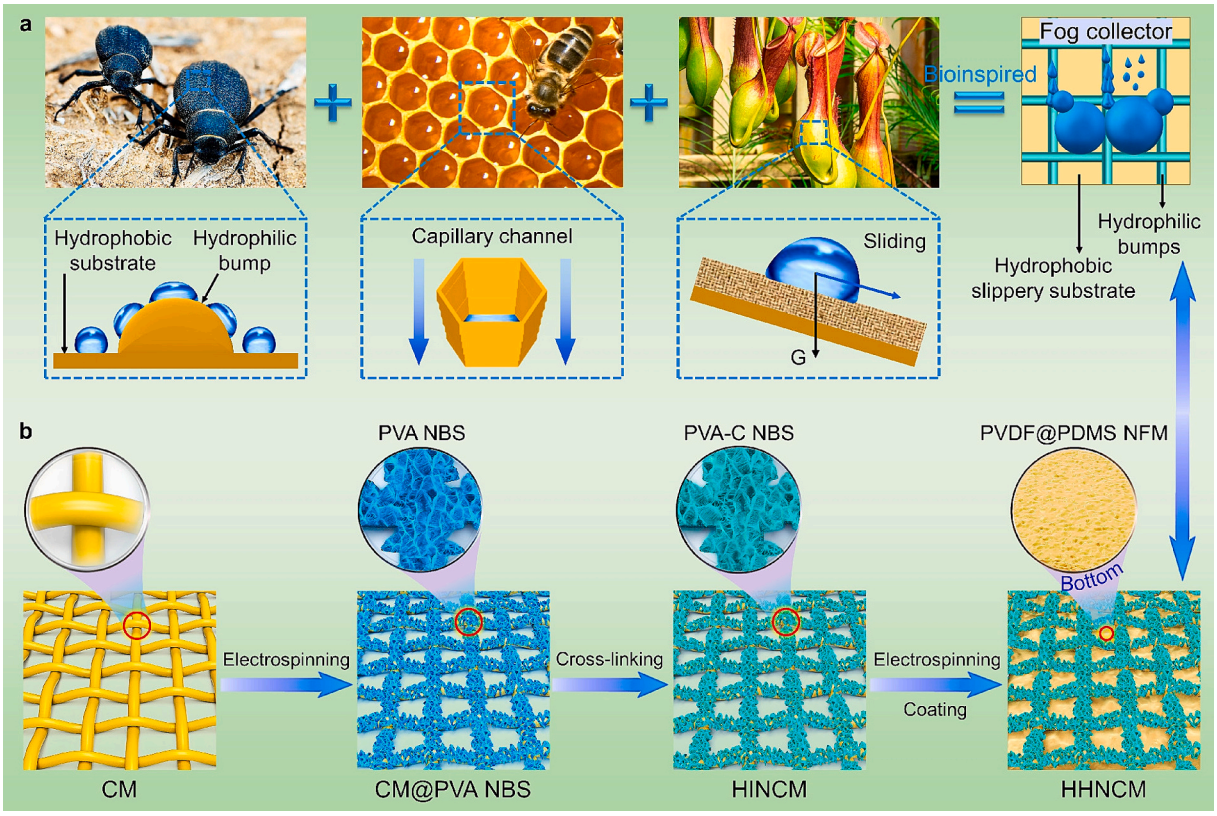

Fig. 17. Bioinspired hybrid surface: (a) Namib Desert beetle and (b) pitcher plant structures (Zhang et al., 2021a).

values to polytetrafluoroethylene, but none of the tested materials showed a sufficiently high level of anti-icing behavior. Quasicrystals-2 showed only a slight improvement over AA6061 in ice accumulation but had higher ice stickiness.

Piscitelli (Piscitelli, 2022) determined the effectiveness of SHS coatings in reducing ice formation under actual flight icing conditions. The researchers tested two SHS coatings at speeds of 50 and 95 m/s and temperatures ranging from −3 to −23 °C. They found that the effectiveness of the coatings largely depended on the testing conditions, with lower ice accumulation achieved in glaze ice conditions and shorter exposure times. However, for use in a wide range of flight icing conditions and long exposure times, these coatings must be considered as a support to an active system.

Rivero et al. (Rivero et al., 2020) focused on the development of passive solutions for preventing ice accretion on aircraft, including various anti-icing coatings tested for hydrophobic properties and effectiveness in a laboratory scale icing wind tunnel. Tests were conducted for ice accretion, durability of anti-icing behavior after multiple cycles, and ice adhesion. All coatings showed significant anti-icing behavior, with some maintaining effectiveness for over 25cycles, providing insights for future developments and validating laboratory scale tests.

Liu et al. (Liu et al., 2018) presented a comparison of a propeller model's normalized thrust coefficients (normalized by thrust coefficients for the scenario in which there was no ice accumulation on the propeller surface) and a conventional propeller model's thrust coefficients (Fig. 15). Brandt and Selig (Brandt and Selig, 2011) developed the following equation to describe the thrust coefficient (C_T) of a propeller:

$$C_T = \frac{T}{\rho n^2 D^4}$$

The variables in this equation represent the propeller's rotational speed (n), diameter (D), air density (ρ), and thrust force (T).

Uneven icicle accumulation and the movement of surface water were examined in the test scenario with a hydrophilic propeller surface, as previously described. For the test situation in which the propeller surface was hydrophobic coatings, surface water movement and uneven icicle accumulation (i.e., the Surface-I case) were observed. Icicle formations along the rotor blades caused the streamlined profiles of the propeller blades to be significantly distorted, resulting in a considerable reduction in the aerodynamic efficiency of the propeller blades (i.e., the lift decreased and drag increased). In the study, it was observed that the thrust generated by the propeller model with a HS (i.e., the Surface-I case) decreased rapidly; this is evident in Fig. 15. The increasing number of super-cooled water droplets hitting the propeller surface led to the formation of complex icicle structures resembling lobster tails. Approximately 70 s into the ice accretion experiment, the thrust coefficient was found to become negative, signifying a complete loss of the propeller model's ability to generate thrust. Due to heavy ice accumulation, the propeller operated in "drag generation mode" instead of the intended "thrust generation mode," causing a significant increase in drag and slowing down the unmanned aerial systems.

Song et al. (Song et al., 2015a) studied the wetting states of droplets on partially micro-grooved surfaces created using soft lithography. According to them, a droplet impinging on these slightly grooved surfaces spreads much like that on a flat surface. However, the recoiling mechanism was very anisotropic. They increased the recoil velocity as long as the recoil was parallel to the grooves; if the recoil was not parallel to the grooves, they decreased the recoil velocity. As the percentage of grooved area increased, the recoiling mechanism became more anisotropic. Surface topographies and scanning electron microscope images of machined micro-grooves were obtained by Cheng et al. (Cheng et al., 2020), as shown in Fig. 16. When the ratio of the wet projection to the total projection area was the same, the groove spacing and width had a significant effect on sliding angles and durations in the same direction of the surfaces.

Sarshar et al. (Sarshar et al., 2018) examined the effectiveness of

Table 3
Surfaces with Hybrid Wettability.

CA, °	Fabrication methodology	Applications	Reference
0–100	Vapor diffusion	Steam condensation	(Daniel et al., 2001)
0–105	Photolithography, deep reactive ion etching, and oxygen-based plasma	Droplet splitting	(Jokinen et al., 2008)
5–164	Gradual substrate move (layer by layer deposition)	Rewritable and switchable wetting	(Wang et al., 2010b)
52–100	Vapor diffusion	Steam condensation and drop distribution shift	(Macner et al., 2014)
118–150	Photolithography, reactive, and deep reactive ion etching	Droplet positioning and coalescence- induced motion	(Li et al., 2014)
39–151	Photolithography, plasma etching, and gradual solution rise	Water droplet manipulation	(Lai et al., 2010)
31–104	Electrochemical oxidation	Water droplet manipulation	(Deng et al., 2017)
53–135	Photolithography and UV treatment	Water droplet manipulation, metering, and merging	(Wu et al., 2017)
100–140	Photolithography and plasma etching	Underwater air bubble manipulation	(Chen et al., 2018)
60–120	Ultraviolet-ozone treatment	Water collection	(Gurera and Bhushan, 2019)
0–84	CO2-based laser drilling	Sweat droplet transportation and thermal management of the human body	(Dai et al., 2019)
108–165	Photolithography, reactive ion etching, and oil infusion	Water droplet manipulation (uphill and straight mobility)	(Launay et al., 2020)
68–162	Laser cutting	Electrolysis and gas collection	(Xiao et al., 2021)
100–150	–	Droplet motion on linear wettability gradient surface in microgravity environment	(Baghel and Ranjan, 2022)

SHSs with different surface roughness and wettabilities for both anti-icing and deicing purposes. Their research showed that while a SHS with a lower depinning force (also known as contact angle hysteresis) can effectively delay ice accumulation in dynamic conditions, it may need a higher shear adhesion force to prevent ice formation in static conditions where factors such as condensation and droplet wetting state play a more significant role.

In summary, while SHSs can prevent the initial formation of ice, they may not be effective in preventing the adhesion of ice that has already formed due to the higher surface energy of ice. Additionally, increasing surface roughness can improve hydrophobicity, but it can also increase ice adhesion at low temperatures (Cui and Pakkanen, 2020; Kim et al., 2020). To combat this issue, scientists and engineers have explored injecting lubricating oil into SHSs, inspired by lubricating fluids secreted by some soft animals and plants (Carlotti et al., 2021). These surfaces have self-healing and durability properties that can remove condensation from the surface. However, the release of lubrication layers may pose environmental hazards (Feng et al., 2022; Zhuo et al., 2021). To overcome the limitations of SHSs, the use of hybrid surfaces that combine superhydrophobic and hydrophilic (wettability gradient) coatings is a promising technique. Historically, the identification of a wettability gradient dates back to 1967 when Carter first discovered the self-mobility of a biological cell. This was followed by further attempts to understand its mechanism by Greenspan in 1978 (through modeling and experiments) (Greenspan, 1978), as well as by Brochard in 1989 (through modeling)(Brochard, 1989). These attempts were later experimentally demonstrated with explicit evidence by Chaudhury and Whitesides in 1992 (Chaudhury and Whitesides, 1992). It is of broad importance to emphasize the gradient in surface science, which is defined herein as the spatial variable of a surface parameter with a magnitude and certain direction.

This approach can be an effective strategy to address the shortcomings of SHSs in anti-icing applications. The hydrophilic component of the surface can attract water molecules and facilitate ice removal, while the superhydrophobic component can prevent water droplets from sticking to the surface and inhibit ice formation. By activating the hydrophilic portion of the surface due to high surface energy, the adhesive forces between the ice and the surface can be reduced, making it easier to remove the ice.

6. Natural superhydrophilic-superhydrophobic hybrid surfaces

Plants such as *Alchemilla mollis* and *Euphorbia* have SHS and HS leaves, with the central parts of their leaves being particularly hydrophilic. This is due to the structures and chemistry of these surfaces, which allow for water accumulation due to the presence of SHS areas with a high adhesive state. An example of this is seen on the surface of a red rose. When the droplet reaches a certain level, the leaves of this plant twist and direct the droplets towards its stem. A similar mechanism has been observed in Namib Desert insects, which use an SHS waxy coating with hydrophilic areas to direct large droplets to their mouths. The cactus *Opuntia microdasys*, which grows in the Chiu Wahwa Desert, collects water from fog with its razor-like blades (Fig. 17), which have microspores at their tips that create variable wettability. The native grass of the Namib Desert, Stipagrostis sabulicola, also has grooves on its axis that guide water (Darmanin and Guittard, 2015; Yin et al., 2017). The Cotula fallax collects fog water due to the three-dimensional placement of its delicate leaves and hairs. The Sri Lankan spider *Uloborus walckenaerius* collects fog water with silk consisting of twisted knots of nanofibrils. This pattern of surfaces with both hydrophobic and hydrophilic properties is commonly known as hybrid surfaces (Darmanin and Guittard, 2015; Yin et al., 2017).

Hybrid surfaces can funcion as an anti-icing passive system on aircraft surfaces, exerting control over ice formation and delaying or inhibiting ice nucleation. Various methods for leveraging hybrid surfaces for anti-icing are detailed below:

1) Directing water droplets towards an area where they can be swept away: Superhydrophobic areas on hybrid surfaces have the ability to repel water droplets, thereby preventing adherence to the surface and facilitating droplet shedding (Jiang et al., 2023; Zhou et al., 2021).
2) Utilizing hydrophilic areas to channel water droplets towards a designated removal point, such as a drainage system or a wiper blade (Zhou et al., 2021).
3) Delaying or inhibiting ice formation: The synergistic effects of hydrophilic and superhydrophobic regions on the hybrid surface contribute to a delay or inhibition of ice nucleation. Specifically, the hydrophilic regions facilitate uniform water droplet nucleation and growth, while superhydrophobic regions promote droplet shedding and minimize the contact area with the droplets (Jiang et al., 2023; Zhou et al., 2021). Such delay or inhibition can diminish the necessity for active de-icing systems, thereby enhancing anti-icing efficiency.
4) Manipulating the spreading factor: By strategically designing hydrophilic and superhydrophobic regions, hybrid surfaces can control the spreading factor, a quantitative measure of a surface's wettability. This control allows for optimization in terms of droplet shedding and direction towards an area where removal is facilitated (Jiang et al., 2023; Zhou et al., 2021).

Recently, various synthetic hybrid surfaces have been developed that

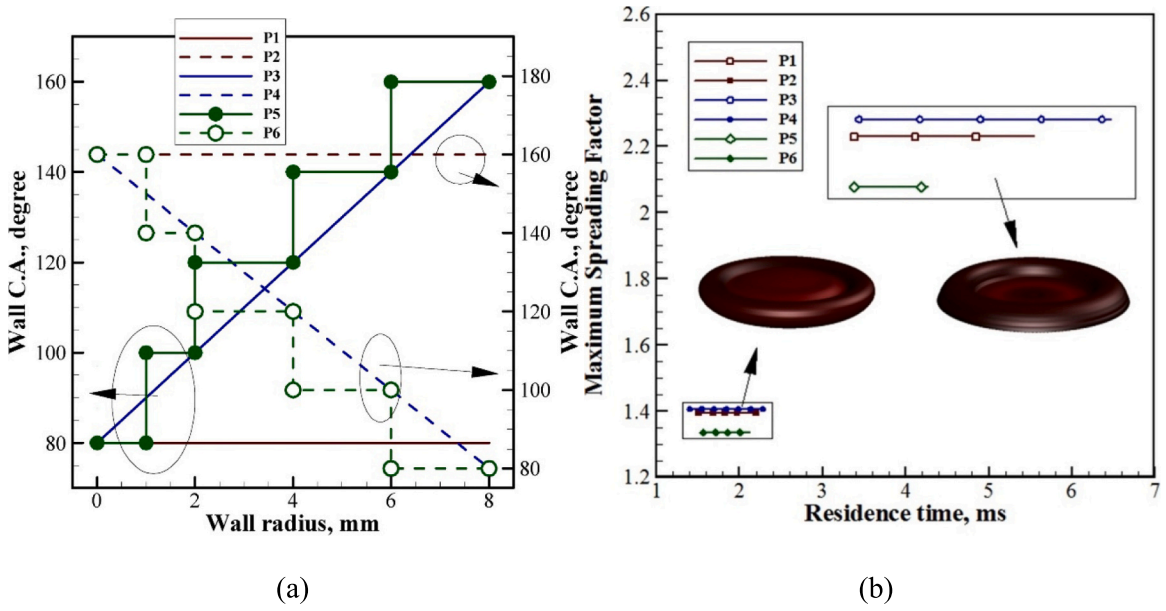

Fig. 18. Effects of (a) various CA distributions on (b) water droplet behavior (Sotoudeh et al., 2021).

combine both hydrophilic and superhydrophobic coatings. These are designed for a myriad of applications, leveraging their distinctive characteristics that permit the concurrent use of both surface properties (Mousavi et al., 2023; Mousavi and Lee, 2022; Mousavi and Roohi, 2023; Mousavi et al., 2022; Sotoudeh et al., 2021; Sotoudeh et al., 2023). Table 3 delves into a variety of surfaces exhibiting hybrid wettability, showcasing their diverse CA ranges, fabrication methodologies, and applications. For instance, surfaces with a CA range between 0 and 100° are created using vapor diffusion and are primarily utilized in steam condensation (Daniel et al., 2001). Another remarkable technique, involving photolithography combined with deep reactive ion etching and oxygen-based plasma, produces surfaces that exhibit a CA between 0 and 105°, which are beneficial in droplet splitting applications (Jokinen et al., 2008). Gradual substrate move (layer by layer deposition) yields surfaces with a wider CA range of 5–164°, offering innovative functionalities such as rewritable and switchable wetting (Wang et al., 2010b). Notably, methods like photolithography, reactive, and deep reactive ion etching produce surfaces with CAs from 118 to 150° that are adept at droplet positioning and the coalescence-induced motion (Li et al., 2014). We also observe intricate applications like sweat droplet transportation and thermal management of the human body using surfaces with a CA of 0–84°, fabricated via CO2-based laser drilling (Dai et al., 2019). Moreover, the table highlights surfaces specifically tailored for underwater air bubble manipulation, electrolysis, gas collection, and even the movement of droplets in microgravity environments (Baghel and Ranjan, 2022; Chen et al., 2018; Xiao et al., 2021). The diversified fabrication techniques and the breadth of applications underscore the immense potential and adaptability of hybrid surfaces.

6.1. *Synthetic hybrid surface*

Generally, the behavior of droplets on solid surfaces displaced by a shear flow has been intensively investigated not only because of its significance in fundamental research but also because of its relevance in droplet-based devices in industrial applications such as chemical sensors, microfluidics, and microreactors. Electrowetting-on-dielectric and thermocapillary are two techniques that have been developed to create wetable gradient surfaces via physical microstructure, chemical reactions, or the application of external fields. Wetable gradient surfaces are the most commonly used in these applications for guiding the droplet. The hybrid surfaces promote interaction between hydrophilic and hydrophobic forces, leading to the speeding up of droplets rebounding from the surfaces, unlike both homogeneous hydrophilic and SHSs. Fig. 18 shows the effects of various CA patterns (Fig. 18a) on a solid surface on the maximum spreading and residence time of water droplet. Evidently, the minimum residence time can be achieved through a stepwise distribution of CA, ranging from SHS (high CA) to

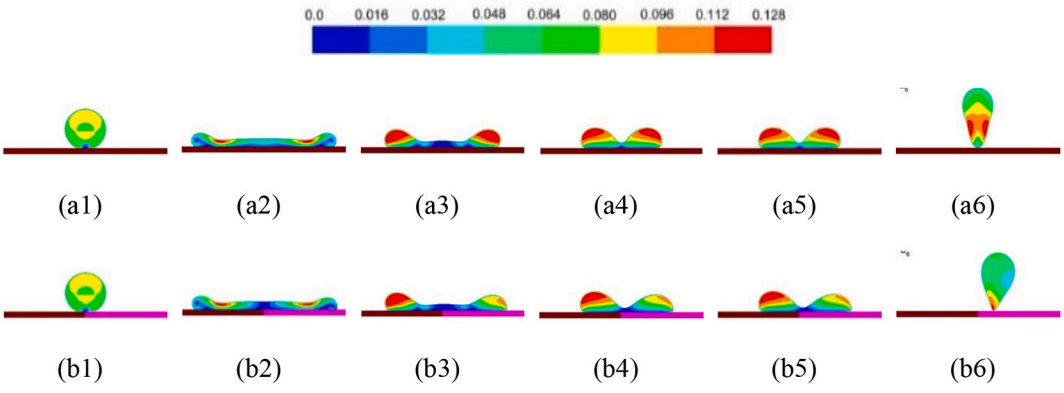

Fig. 19. Dynamic droplet behaviors during the impact with (a1–a6) surface with a CA of 150°, and (b1–b6) a hybrid surface with the contact angles 150° and 120°.

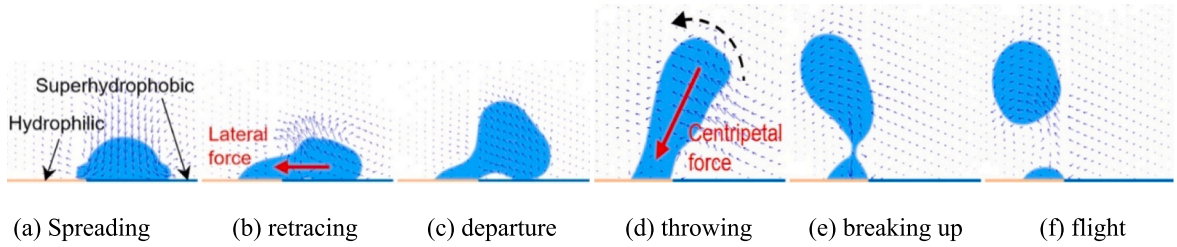

Fig. 20. Comparison of the droplet dynamic behavior at collision between homogeneous and hybrid surfaces (Chu et al., 2020).

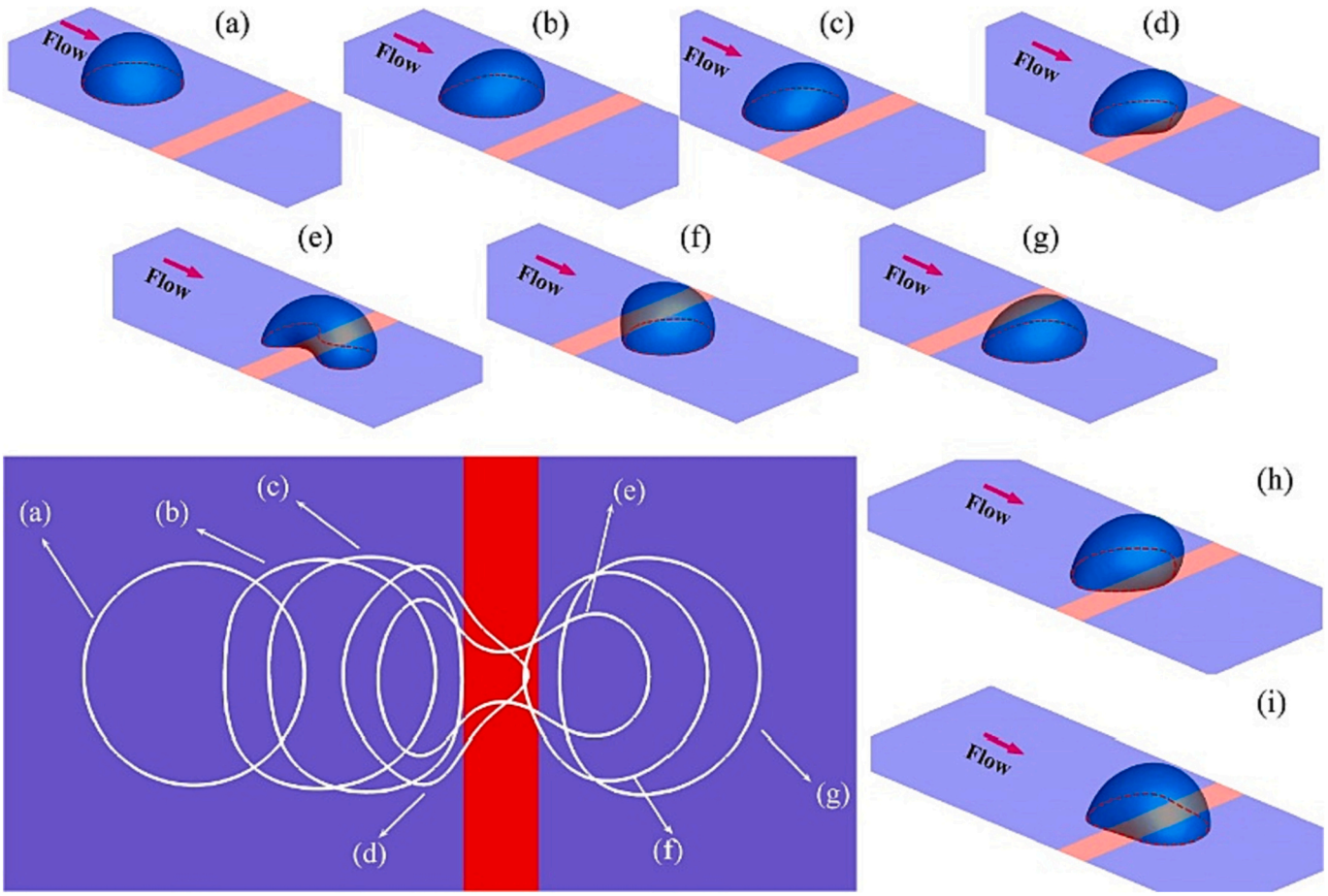

Fig. 21. Shape and contact line profiles during the passage of a droplet through the wetting defect (stripe-like areas) with (a)–(g) ($\Delta\theta_e$, θ_1) = (5π/18, 0.5π), and (h, i) ($\Delta\theta_e$, θ_1) = (3π/18, 0.5π) (Shang et al., 2019).

hydrophilic (low CA) surfaces (Sotoudeh et al., 2021).

It should be noted that Yuan et al. (Yuan et al., 2020) observed that when a droplet impinges on a surface with a wettability difference, it undergoes a different set of phases compared to impinging on homogeneous surfaces. These phases include asymmetric spreading, retracting, detaching, and migrating. The droplet's asymmetric spreading behavior is due to an unbalanced net force in the lateral direction. As the liquid rapidly retracts in the hydrophobic area, it results in directional rebounding towards the wetter region. The increase in wettability difference causes the contact line to move farther, reduces the droplet's bouncing height, and shortens the contact time between the liquid and non-wetting area (Yuan et al., 2020).

A study conducted by Ji et al. (Ji et al., 2021) compared the contact processes of a drop impacting on homogeneous and heterogeneous surfaces. Fig. 19 (a1-a6) shows the change in momentum modulus when the drop falls on a homogeneous surface with a contact angle of 150°, with each subfigure representing the momentum at different times. The drop spreads rapidly, with its kinetic energy being partly transformed into interfacial energy, and then retracts to reduce its interfacial energy. On a heterogeneous surface with a configuration of 150°-120°, Fig. 19 (b1-b6) shows that the drop spreads rapidly at first, reaching a maximum spreading diameter after 1.35 ms. During the recoiling process, the left side of the drop recoils more quickly due to the heterogeneity of the surface. The drop is asymmetric throughout the spreading and recoiling processes on the chemically heterogeneous surface, and the changes in its internal momentum modulus are also asymmetrically distributed. The drop spreads and recoils on the substrate at a constant contact angle, and its center of mass deviates from the central position of the substrate. If the dissipation within the drop and friction with the surface are sufficiently low, the drop will have enough energy to rebound.

Fig. 20 compares the droplet behavior at collision between a surface with a homogenous CA and a surface with a hybrid CA pattern (Chu et al., 2020). As shown, the droplet wets less area of the hybrid surface,

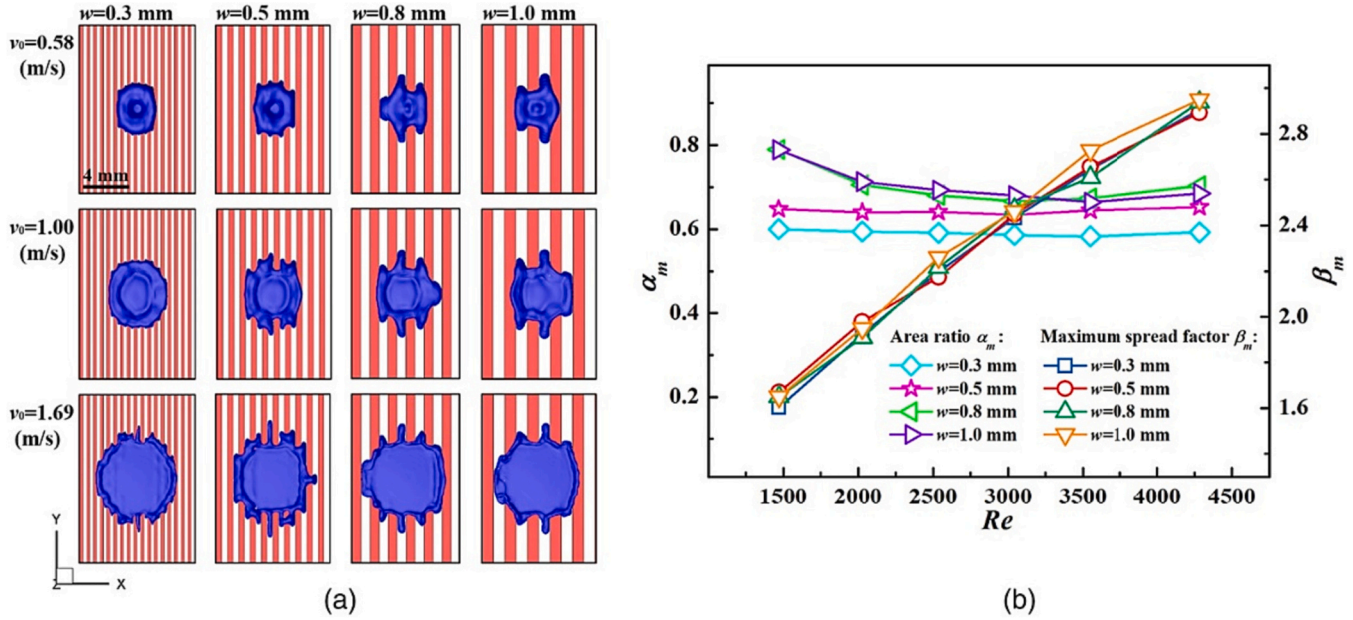

Fig. 22. Two aspects of droplet behavior at the point of maximum spreading: (a) changes in the shape of the droplet with varying widths of the stripe (*w* ranging from 0.3 to 1.0 mm), and (b) comparison of the area ratio (α_m) and maximum spread factor (β_m) for different Reynolds numbers (Zou et al., 2020).

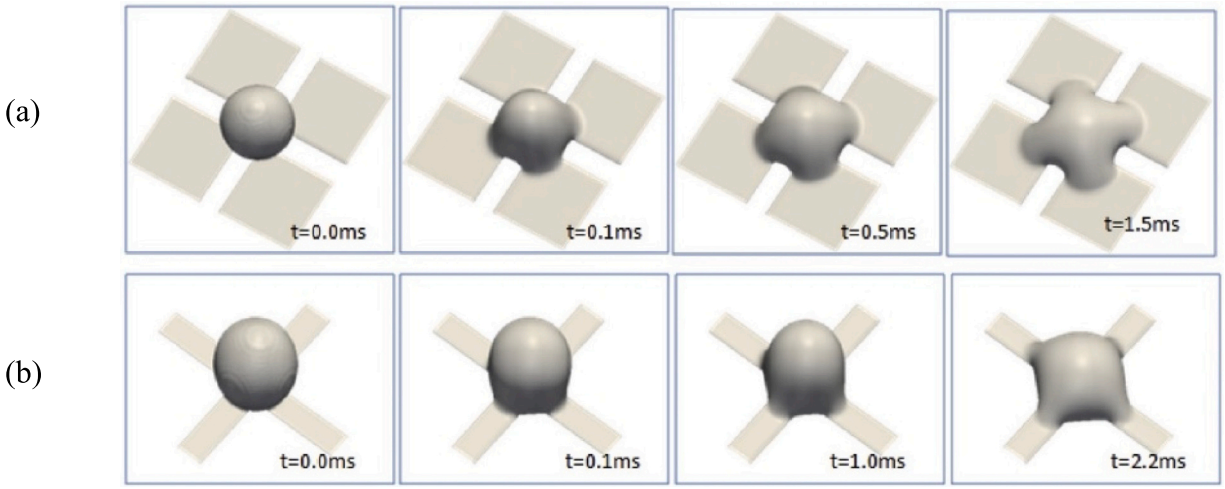

Fig. 23. Spreading of a droplet on hydrophilic strips on (a) Cross shaped and (b) inverted cross shaped strips (Pravinraj and Patrikar, 2019).

implying that when hybrid surfaces are used, the residence time of the droplet is lower. A reduction in the residence time of the droplet reduces the heat transfer from the surface to the droplet, which impedes the icing phenomenon.

Wettable gradient surfaces are commonly used to guide droplets and find application in various fields such as chemical sensors, microfluidics, and microreactors(Shang et al., 2019). Fig. 21 displays snapshots of the droplet and contact line that demonstrate their positions above the critical trapping condition (Shang et al., 2019). Droplets initially reach this condition, represented in Fig. 21, before they enter the wetting defect (c). Then, a portion of the downstream contact line begins to enter the defect. Fig. 21 shows that when the contact line enters the defect, a central protuberance (d) and (h) emerges and grows as a result of the imbalanced interfacial force at the defect's contact line, pulling the droplet into the defect in a direction that is parallel to the defect. If the defect has high strength, the contact line's leading edge is extremely sharp (d). The force acting on the contact line elongates the droplet outward, preventing the contact line from retreating after the contact line has passed through the wetting defect, as shown in Fig. 21e. Microfluidic droplet formation employing a flow-focusing junction is comparable to the squeezing of a droplet perpendicular to the flow direction. A bullet-shaped contact line is used to pass the droplet through a defect of low strength, as shown in Fig. 21i. When the CA difference increases (e.g., e = 5/18 in Fig. 21e), a thin bridge linking the two ends of the contact line appears (i.e., Fig. 21g). This process continues until the entire contact line passes through the wetting defect. Droplets striking a single flaw on a HS have been shown to exhibit similar behavior. Because of the high imbalanced interfacial tension, the wetting defect can function as a blade and potentially cut the droplet into half. This is the case with most wetting defects.

Fig. 22a indicates that the droplet shape is axisymmetric when it hits the center of either the hydrophilic or hydrophobic stripe. Fig. 22b illustrates the changes in the area ratio (α_m) which ratio of the contact area between liquid and solid on the SH side to the overall contact area, along with the maximum spread factor (β_m), varies with Reynolds number. The figure demonstrates that α_m remains constant regardless of

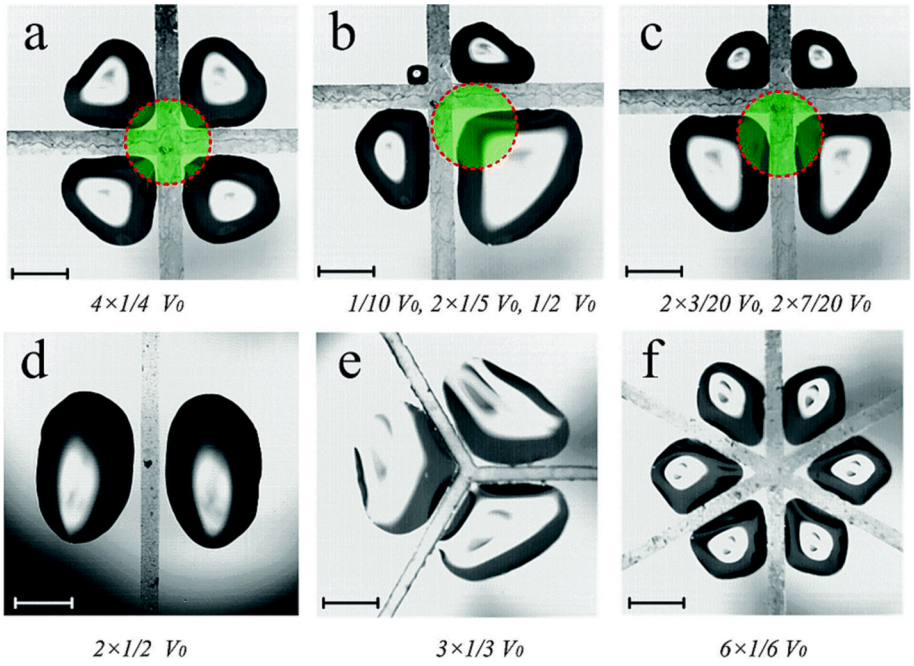

Fig. 24. Droplet behavior upon collision with hybrid surfaces (Song et al., 2015b).

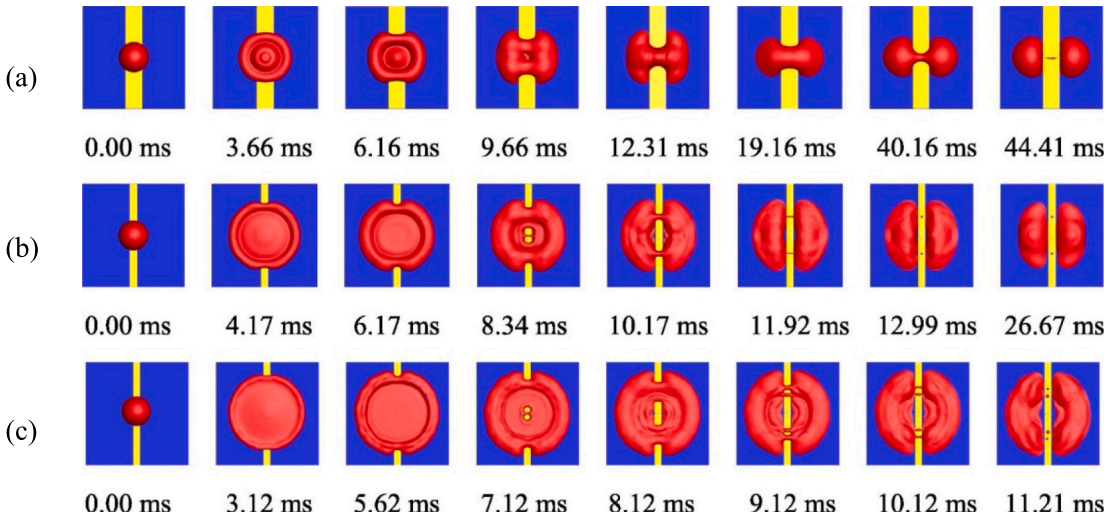

Fig. 25. Structure of droplet split with an SHS strip: (a) Single-liquid-bridge formation and rupture, (b) double-liquid-bridge formation and rupture, and (c) quadruple-liquid-bridge formation and rupture (Wang et al., 2019).

the point of impact, while β_m increases with increasing Reynolds number. The variation in the maximum spread factor between various impact points is minor for the same impact velocity (Zou et al., 2020).

To use the effects of strips (of different wettability) on droplet behaviors, many scholars have applied a stripe on the surface to control the droplet shape and structure. It has been shown that the droplet size and stripe width have a significant effect on the droplet motion. The sliding droplet should have sufficient kinetic energy to overcome the energy barrier generated by the stripes with greater hydrophobicity and enter the stripes. A tiny droplet has a glide-only motion since it lacks kinetic energy and will be prevented by the stripes' boundary. While a droplet with a bigger diameter may still cross the stripes irrespective of how wide they are, a wider stripe increases the gliding distance and causes a glide-cross motion to be generated. The stripe width can be used to send droplets of various radii in the desired direction.

As shown in Fig. 23a, the spreading of a 25-μm droplet across a cross-shaped strip has also been studied (Pravinraj and Patrikar, 2019). Each strip had a width of 10-μm and was placed at the center of the lattice domain at a distance of 120× 80 × 120. Approximately 45% of the total surface area was hydrophilic. After starting out as a cap-like structure, the droplet finally extended across four HSs in a bow-neck shape. Moreover, previously hydrophobic strips were inverted to become hydrophilic, whereas all other regions of the surface remained hydrophobic. After a while, as evident in Fig. 23, the droplet followed a cross-shaped hydrophilic strip (b). These findings show that droplets may be formed in a controlled manner without the need for an external force by using the internal surface force. A partial wetting surface for the splitting procedure could also be realized owing to this finding.

Fig. 24 shows how collisions with SHS striped hybrid surfaces can produce additional interesting consequences (Song et al., 2015b). With the help of SHS stripes, the droplets in this experiment formed mini-marbles mini-marbles (Fig. 24 a-c). In order to manage the volume

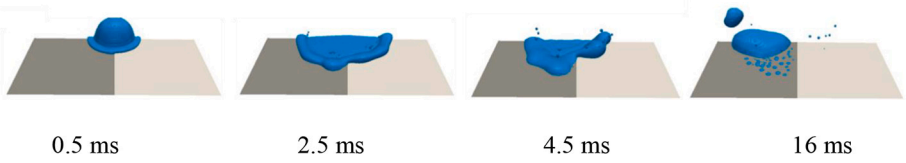

Fig. 26. Droplet impiniging on a wettability step. CA of dark-grey zone (HS) is 89°, $\theta_a = 93°$, and $\theta_r = 0°$, and the CA of the light-grey zone (SHS) is 159°, $\theta_a = 166°$, and $\theta_r = 155°$ (Russo et al., 2020).

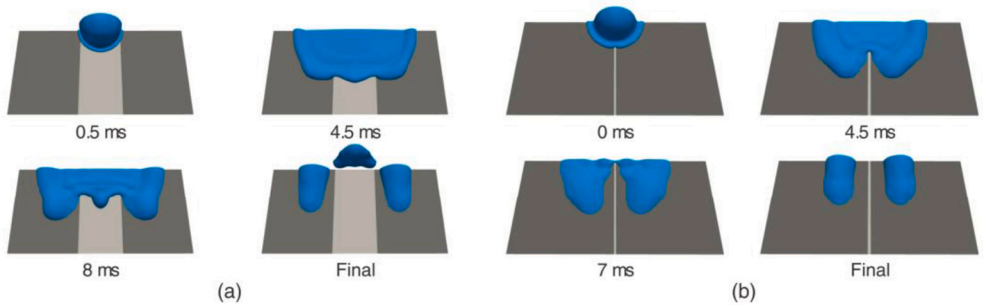

Fig. 27. Droplet collision with *We* number of 60 on surfaces with various wettability patterns comprising hydrophilic ($\theta_0 = 89°$, $\theta_a = 93°$, and $\theta_r = 0°$) surfaces (in dark grey) surrounding SHS ($\theta_0 = 159°$, $\theta_a = 166°$, and $\theta_r = 155°$) strips (in light grey) of widths (a) 3 mm and (b) 0.2 mm (Russo et al., 2020).

fractions of the droplets, the researchers adjusted the landing point. Using red dots and green shadows, they could find the droplet's size and location, and (Fig. 24 d-f) many mini-marbles were formed from raindrops.

Wang et al. (Wang et al., 2019) reported that droplets can be split into two symmetric parts with correct strip width and wettability contrast, at all Weber numbers (*We*), including low, moderate, and high *We* numbers of 15, 40, and 65. This is due to the non-axisymmetric motion of the film on the strip that causes non-axisymmetric spreading and retraction, unlike a liquid bridge formed on a HS that reduces viscous dissipation. Fig. 25(a–c) displays snapshots of droplets striking mixed-wettability surfaces for splitting states (hydrophobic strip placed on a hydrophilic background surface) under three different wetting conditions, as shown in Fig. 25(c). The retraction velocity is higher for a greater *We*, higher wettability contrast between the HS and the hydrophobic strip, and broader strip. The film on the strip transforms into a liquid bridge in a shorter period than in non-splitting situations, owing to quicker retraction. Consequently, the droplet divides into two halves that evolve independently on both sides of the HS. This results in rupture of the liquid bridge, which can be single, double, or quadruple, depending on strip width, Weber number, and wettability contrast between the strip and the liquid. Specifically, single-liquid-bridge rupture occurs only under specific conditions, i.e., low *We* (15), minimal wettability contrast (115°), and large strip width (1.75 mm). In contrast, eight quadruple-liquid-bridge ruptures can be observed at a high We (65) with greater wettability contrast and/or a wider strip. Double-liquid-bridge rupture occurs for all ranges of wettabilities at a *We* of 40. This is due to air entrainment when a droplet contacts a solid surface, as shown in Fig. 25b and c, where the air layer trapped under the droplet destabilizes and drains away, causing the film on the strip to rupture and produce two or four liquid bridges.

Fig. 26 depicts the interaction between the impacting liquid and each of the exposed surfaces. On the HS side, the maximum spreading is comparable to that of an evenly HS (Russo et al., 2020). For impacts on a surface with a consistent SHS, a similar maximum spread is projected. This result makes intuitive sense, even when the droplet impacts a multiregional wettability surface; in this case, the liquid covering each zone does not experience the matching influences of the other half section, and therefore the liquid spreading unravels as if each surface were independent. The SHS aids in retraction when lateral spreading has

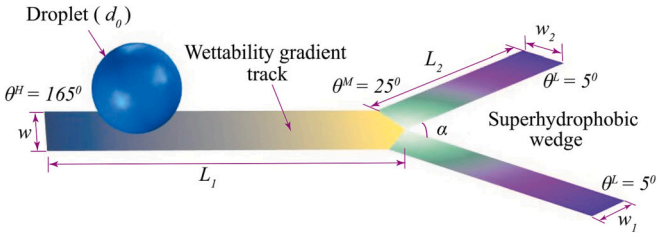

Fig. 28. Configuration of the Y junction with hybrid CA (Chowdhury et al., 2021b).

reached its maximum. When the droplet is anchored over the HS, the retreating fluid's energy is directed towards the HS side, which finally causes the entire fluid to enter the HS side. However, although the droplet stays pinned as a whole, there is sufficient energy in the receding fluid to cause a partial rebound.

The width of the SHS strip has been shown to influence the final form of the impinging liquid and the amount of liquid that bounces off the surface (Russo et al., 2020). Images in Fig. 27a and b indicate the droplet impact at the center of three-millimeter- and two-hundred-micrometer-broad SHS strips. When the droplet impinges on the broader (3 mm) strip, it partially rebounds, but not on the 0.2 mm strip. During the impact, several factors such as the maximum spreading factor and droplet form have been examined. The observation that the spreading factor for impacts on SHSs follows a trend similar to that observed in the direction parallel to the strip is fascinating. After reaching a minimal value just prior to droplet detachment, the spreading factor perpendicular to the strip begins to increase again, whereas the spreading factor parallel to the strip begins to decrease after the maximum spreading (Russo et al., 2020).

Fig. 28 depicts a Y-shaped wettability gradient (non-hemogenous wall CA) track that has been set on a SHS backdrop to demonstrate wettability. Evidently, wettability gradient tracks are built on top of SHSs to see what happens when droplets of different sizes are added to the tracks (Chowdhury et al., 2021b). This way, we can see how splitting happens. Splitting of droplets occurs more quickly at an SHS wedge angle of 90°, and the splitting ratio (the ratio between the sizes of the daughter droplets) is influenced by the Y junction widths. At a certain

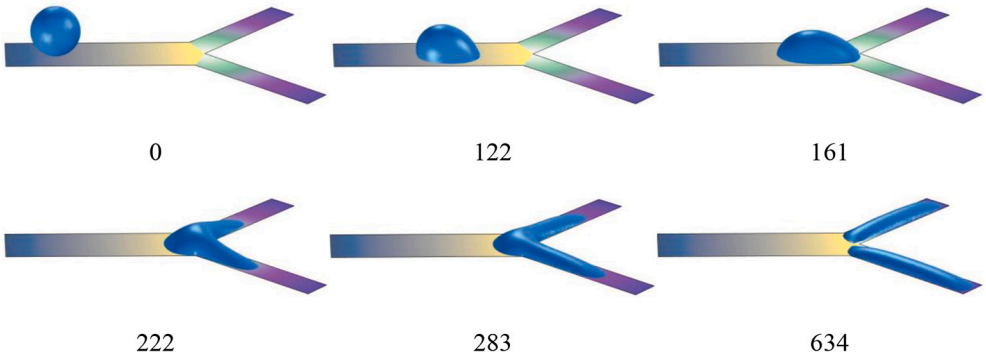

Fig. 29. Droplet splitting on a Y-shaped bifurcated wettability gradient track (Chowdhury et al., 2021b).

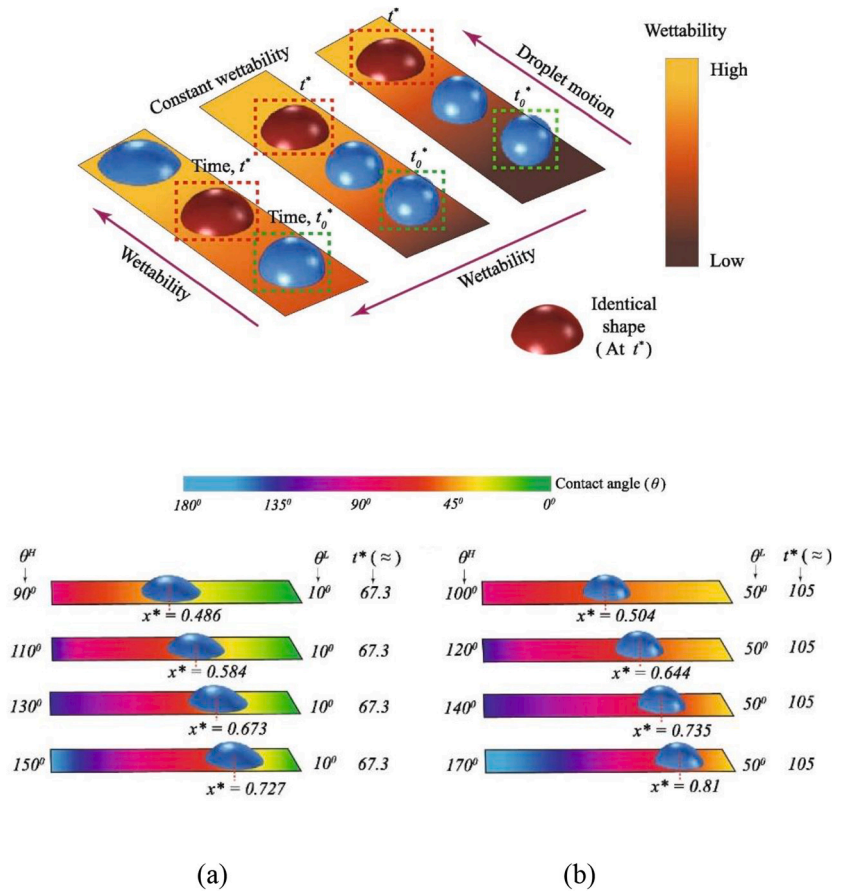

Fig. 30. a. Qualitative representation of identical droplet shape at t* on different wettability gradient surfaces (Chowdhury et al., 2021a).
b. The 0.5 mm glycerin droplets located on surfaces with various wettability patterns with length (*L*) of 3.5 mm (Chowdhury et al., 2021a).

branch-width ratio, the droplet does not divide, but instead moves towards the branch with a larger width and stops in its vicinity. Droplets are placed on the bifurcated wettability gradient track set on an SHS backdrop (Fig. 28). The wettability gradients on the base track (L1) and the Y track branches (L_2) differ. There is a CA of 170° between the Y track's SHS backdrop and the skin. At a distance d_0 (droplet diameter = 0.5 mm) from the left, the droplet's original location is known. There is an SHS wedge that divides the base track of the Y-shaped wettability gradient track into two branches, each with a width of w. The width of the Y track's branches is either w_1 or w_2. The base track of the Y-shape has a length L_1 of 2 mm, while the branches have a length L_2 of 1.5 mm. L_1 shows a linear increase in wettability from $\theta^H = 165^\circ$ to $\theta^M = 25^\circ$, whereas L_2 shows an increase from $\theta^M = 25^\circ$ to $\theta^L = 5^\circ$. The yellow color at the base track and the light green color at the branches indicate that the CA at the bifurcation area is close to 25°. The base track can be clearly distinguished from the branches by the change in color from yellow to light green.

The driving force behind droplet motion in wettability gradients is the difference in curvature between the front and rear halves of the droplet. Fig. 29 demonstrates the droplet splitting dynamics for $w_2/w_1 = 1$ and $\alpha = 90^\circ$. At $t^* = 161$, which represents a nondimensional time, the droplet's wettability improves from left to right, allowing for more stable movement along its base track (length L1), which has a heterogeneous wettability of $\lambda = 0.47$. As the droplet spreads during conveyance, its velocity increases significantly up to $t^* = 161$. However, once it encounters the SHS wedge, despite its poor wettability, the SHS wedge

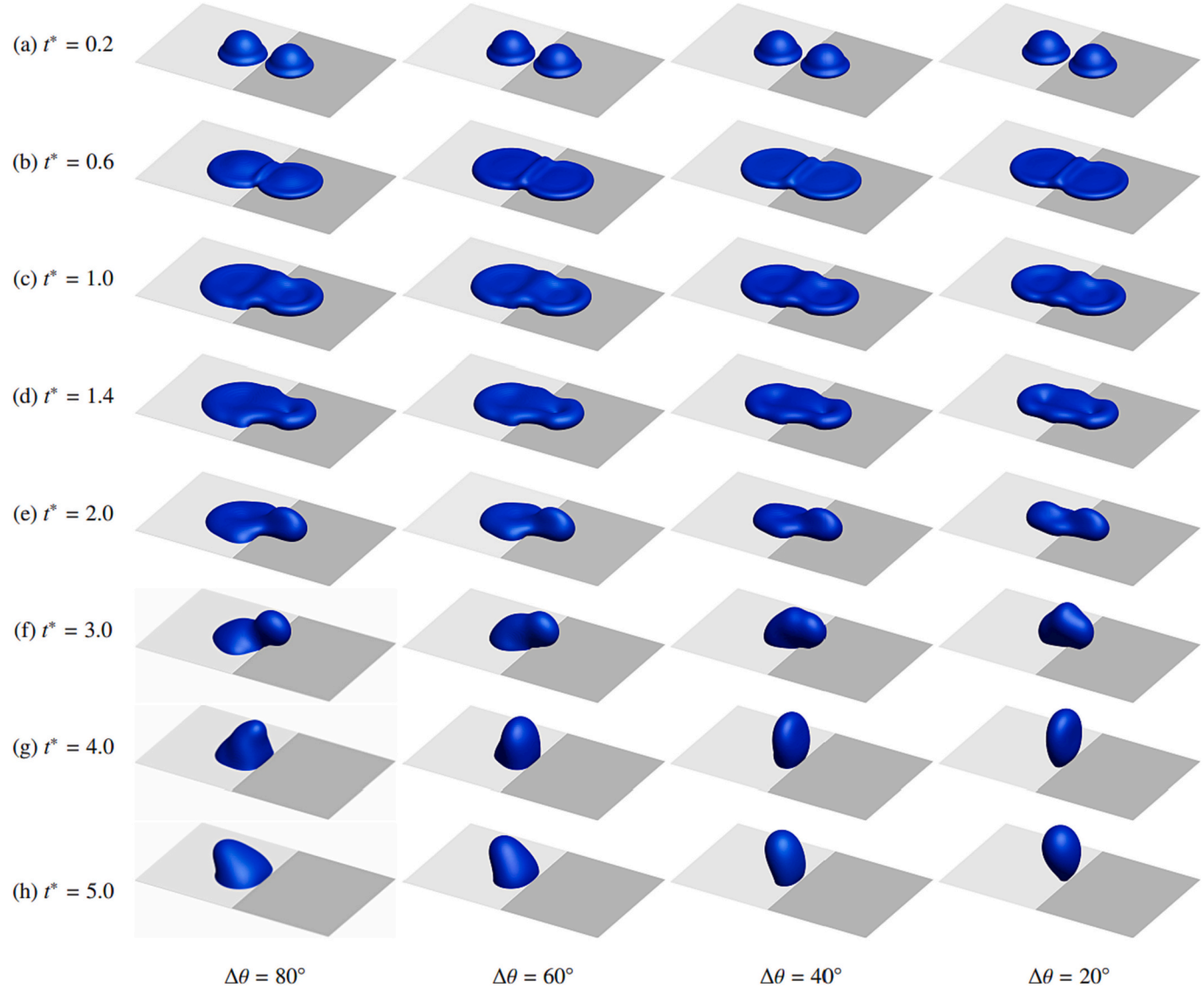

Fig. 31. The dynamic behavior of double droplets impact on hybrid surfaces wettability difference (Δθ) (Huang et al., 2022).

acts as a barrier to the droplet's movement. The driving force generated by the wettability gradient and high wettability in the Y track's branches then causes the droplet to split into two halves along the Y track. The droplet splits between $t^* = 161$ and $t^* = 634$ and divides into two equal volumes since $w_2 = w_1$. The motion and splitting of the droplet are separated into two distinct stages. Stage I is the smooth droplet transport on Y's base track (up to $t^* = 161$), whereas Stage II is the droplet splitting at the SHS wedge ($t^* = 161$).

The same droplet form is shown qualitatively in Fig. 30 for various wetting gradient surfaces (Chowdhury et al., 2021a). It does not matter whether the surface's wettability gradient is steeper (at t_0^*), since the droplet is deposited at the same spot (d_0: distance from the extreme low wettability side) irrespective of which surface it hits. However, the droplet's form remains unchanged at t^*. Fig. 30a shows the droplet at $t^* = 67.3$ at several locations; the droplet's form is the same on all of the tracks. Non-dimensional droplet wetted area (A^*), non-dimensional droplet height (h^*), front CA of the droplet (θ_f), and the back CA of the droplet (θ_r) all indicate the same shape. Using $\theta^L = 10°$, the droplet's A^* is 2.92, h^* is 0.43, θ_f is 46°, and $\theta_r$is 58°. The droplet's uniform shape is determined by the downstream CA (θ^L). Fig. 30b shows a droplet with a form different from that in Fig. 30a because of the existence of two distinct θ^L values. To obtain the same droplet form with $\theta^L = 50°$, the droplet's A^* value is 2, the distance between its sides is 74°, and the distance between its bottom and its top is 83°. For θ^L=10° and θ^L= 50°, the same droplet is formed at $t^* = 67.3$ and $t^* = 105$, respectively. The shape and size of the droplet and t are dependent on the downstream θ^L. This can be observed in Figs. 30a and 30b, which illustrate how the downstream θ^L affects t^*. A 0.5 mm glycerin droplet was transported over a 3.5-mm-long wettability gradient track to investigate this further. The wettability gradient was formed by varying the upstream θ^H, which ranged from 90° to 110°. For any two wettability gradients with a fixed θ^L, the droplet has the same form at the same time after the droplet was inserted on the surface, but at different positions along the base length. Irrespective of how θ^H and θ^L are mixed, the droplet cannot have the same form at the last time of process.

Huanga et al. (Huang et al., 2022) showed that by using hybrid surfaces with various wettabilities, the wetted area could be controllable, and that small differences in CA resulted in the decrease of the spreading factor (Fig. 31).

Hoque et al.(Hoque et al., 2020) created a hybrid surface by coating the microtip's surface with hydrophobic polydimethylsiloxane. In comparison to a uniform SHS, the effectiveness of multi-droplet jumping was nearly 14 times greater. Hou et al. (Hou et al., 2018) created a SHS

with biphilic topography by incorporating patterned wettability with high contrast. The biphilic surface is composed of micropillar arrays with hydrophilic top corners and SHS nanograsses surrounding them. They found that the biphilic surface effectively suppresses ice nucleation more than the hydrophobic and homogeneous super hydrophobic surfaces.

In summary, hybrid surfaces, which combine hydrophilic and superhydrophobic areas, have been found to effectively suppress ice nucleation more than superhydrophobic surfaces alone (Hou et al., 2018; Zhou et al., 2021). The following mechanisms contribute to the reduction or delay of ice accretion on hybrid surfaces:

(a) Disruption of ice nucleation: The combined effects of hydrophilic and superhydrophobic areas on hybrid surfaces create a heterogeneous surface. This heterogeneity disrupts the uniformity required for optimal ice nucleation, making the ice formation process less efficient compared to surfaces that are uniformly wettable (Hou et al., 2018; Zhou et al., 2021). The presence of hydrophilic areas can inhibit ice nucleation by providing sites for water droplet nucleation with uniform rates and sizes (Mishchenko et al., 2013)
(b) Enhanced droplet shedding: The superhydrophobic areas on hybrid surfaces, characterized by micro- or nanostructures, create air pockets and reduce the contact area between water droplets and the surface. This promotes the formation of smaller droplets that are more easily shed from the surface due to reduced adhesion (Hou et al., 2018). The combination of hydrophilic and superhydrophobic areas enhances the droplet shedding capability of hybrid surfaces, further reducing the likelihood of ice accretion (Golovin et al., 2016).
(c) Delayed ice formation: The presence of hydrophilic areas on hybrid surfaces can further enhance the delay in ice formation, potentially due to the uniform nucleation and growth rates of water droplets on the hydrophilic tips (Mishchenko et al., 2013).

7. Challenges

There is a need for further research on hybrid surfaces to address several questions. One key area for future exploration is the effect of surface topography on the anti-icing properties of hybrid surfaces. A main issue in using hybrid surfaces is to use the function of distribution of CA (wettability gradient) on the surface. It is also important to investigate the durability and long-term performance of these surfaces under various environmental conditions.

To evaluate the long-term durability and practicality of hybrid surfaces in real-world applications, research should investigate the effects of environmental factors such as UV radiation, temperature fluctuations, and mechanical wear and tear on the surface properties and performance.

Regarding droplet impact scenarios, future research should focus on understanding the effect of different dimensionless numbers, including Weber and Reynolds numbers (laminar and turbulent flow), on the anti-icing performance of hybrid surfaces. This understanding will aid in optimizing the design of hybrid surfaces for specific applications and in better comprehending the impact and adhesion of droplets on hybrid surfaces.

To achieve optimal performance, specific surface chemistry and topography require investigation and optimization.

8. Concluding remarks

Nature has the potential to bring novel answers to technical difficulties in a wide variety of sectors. This overview summarizes recent achievements, ranging from natural examples to biomimetic surfaces and their functionalities. These surfaces with exceptional wettability qualities have a wide range of possible industrial uses. Several conclusions can be drawn on the basis of the research reviewed:

- Using hybrid surfaces changes the dynamic behaviors of liquid droplets when they collide with the surfaces. These changes include maximum spreading factors, droplet residence time, and the wetted area.
- Using hybrid surfaces breaks droplets out into small parts and prevents them from accumulating in the common shape of the ice, such as rime and glaze ice shapes.

Nevertheless, gaining a fundamental understanding of the anti-icing capabilities of hybrid surfaces, which is essential for precise measurements and extensive modeling, continues to be a challenge. Therefore,

- Further research is needed to look into the effects of different CA patterns on droplet residence time and wetted surface area.
- Surface physical, chemical, thermal, and mechanical properties must also be evaluated in terms of cost-effective processing, durability, and practical applications.

However, the research that is being done to get around these problems and the progress that has been made are encouraging.

Declaration of Competing Interest

The authors declare that they have no known competing financial interests or personal relationships that could have appeared to influence the work reported in this paper.

Data availability

No data was used for the research described in the article.

References

Addy, H., Sheldon, D., Potatpczuk, J.M., Addy, H., Sheldon, D., Potatpczuk, J.M., 1997. Modern Airfoil ice accretions. In: 35th Aerospace Sciences Meeting and Exhibit. Aerospace Sciences Meetings. American Institute of Aeronautics and Astronautics.
Ahmad, M.M., Eshaghi, A., 2018. Fabrication of antireflective superhydrophobic thin film based on the TMMS with self-cleaning and anti-icing properties. Prog. Org. Coat. 122, 199–206.
Antonini, C., Innocenti, M., Horn, T., Marengo, M., Amirfazli, A., 2011. Understanding the effect of superhydrophobic coatings on energy reduction in anti-icing systems. Cold Reg. Sci. Technol. 67 (1), 58–67.
Baghel, V., Ranjan, M., 2022. Numerical estimation of droplet motion on linear wettability gradient surface in microgravity environment. Mater. Today Communicat. 32, 103916.
Banitalebi Dehkordi, H., Farzaneh, M., Van Dyke, P., Kollar, L.E., 2013. The effect of droplet size and liquid water content on ice accretion and aerodynamic coefficients of tower legs. Atmos. Res. 132-133, 362–374.
Bansmer, S.E., Baumert, A., Sattler, S., Knop, I., Leroy, D., Schwarzenboeck, A., Jurkat-Witschas, T., Voigt, C., Pervier, H., Esposito, B., 2018. Design, construction and commissioning of the Braunschweig Icing Wind Tunnel. Atmos. Meas. Tech. 11 (6), 3221–3249.
Barberoglou, M., Zorba, V., Stratakis, E., Spanakis, E., Tzanetakis, P., Anastasiadis, S.H., Fotakis, C., 2009. Bio-inspired water repellent surfaces produced by ultrafast laser structuring of silicon. Appl. Surf. Sci. 255 (10), 5425–5429.
Barthlott, W., Neinhuis, C., 1997. Purity of the sacred lotus, or escape from contamination in biological surfaces. Planta 202 (1), 1–8.
Barthlott, W., Riede, K., Wolter, M., 1994. Mimicry and ultrastructural analogy between the semi-aquatic grasshopper Paulinia acuminata (Orthoptera: Pauliniidae) and its foodplant, the water-fern Salvinia auriculata (Filicatae: Salviniaceae). Amazon.: Limnol. Oecol. Regionalis Systemat. Flumin. Amazon. 13 (1–2), 47–58.
Barthlott, W., Mail, M., Neinhuis, C., 2016. Superhydrophobic hierarchically structured surfaces in biology: evolution, structural principles and biomimetic applications. Philos. Trans. R. Soc. A Math. Phys. Eng. Sci. 374 (2073), 20160191.
Bascom, W.D., Cottington, R.L., Singleterry, C.R., 1969. Ice Adhesion to Hydrophilic and Hydrophobic Surfaces. J. Adhes. 1 (4), 246–263.
Betz, A.R., Jenkins, J., Kim, C.-J.C., Attinger, D., 2013. Boiling heat transfer on superhydrophilic, superhydrophobic, and superbiphilic surfaces. Int. J. Heat Mass Transf. 57 (2), 733–741.
Bhushan, B., Jung, Y.C., 2011. Natural and biomimetic artificial surfaces for superhydrophobicity, self-cleaning, low adhesion, and drag reduction. Prog. Mater. Sci. 56 (1), 1–108.

Bowden, D.T., Gensemer, A., Skeen, C.A., 1964. Engineering Summary of Airframe Icing Technical Data. Federal Aviation Agency.
Brandt, J., Selig, M., 2011. Propeller Performance Data at Low Reynolds Numbers. In: 49th AIAA Aerospace Sciences Meeting Including the New Horizons Forum and Aerospace Exposition. Aerospace Sciences Meetings. American Institute of Aeronautics and Astronautics.
Brochard, F., 1989. Motions of droplets on solid surfaces induced by chemical or thermal gradients. Langmuir 5 (2), 432–438.
Brown, S., Lengaigne, J., Sharifi, N., Pugh, M., Moreau, C., Dolatabadi, A., Martinu, L., Klemberg-Sapieha, J.E., 2020. Durability of superhydrophobic duplex coating systems for aerospace applications. Surf. Coat. Technol. 401, 126249.
Buran, H., 2023. Governing Characteristics of Droplet Solidification. California State University, Long Beach.
Bush, J.W.M., Hu, D.L., Prakash, M., 2007. The Integument of Water-walking Arthropods: form and Function. In: Casas, J., Simpson, S.J. (Eds.), Advances in Insect Physiology. Academic Press, pp. 117–192.
Butt, H.-J., Graf, K., Kappl, M., 2003. Contact Angle Phenomena and Wetting. In: Physics and Chemistry of Interfaces. Wiley, pp. 118–144.
Byun, D., Hong, J., Saputra, Ko J.H., Lee, Y.J., Park, H.C., Byun, B.-K., Lukes, J.R., 2009. Wetting Characteristics of Insect Wing Surfaces. J. Bionic Eng. 6 (1), 63–70.
Cao, Y., Hou, S., 2015. Extension to the Myers Model for Calculation of Three-Dimensional Glaze Icing. J. Aircr. 53 (1), 106–116.
Cao, Y., Huang, J., 2014. New Method for Direct Numerical simulation of Three-Dimensional Ice Accretion. J. Aircr. 52 (2), 650–659.
Cao, Y., Huang, J., Yin, J., 2016. Numerical simulation of three-dimensional ice accretion on an aircraft wing. Int. J. Heat Mass Transf. 92, 34–54.
Cao, Y., Tan, W., Wu, Z., 2018. Aircraft icing: an ongoing threat to aviation safety. Aerosp. Sci. Technol. 75, 353–385.
Carlotti, M., Cesini, I., Mattoli, V., 2021. A simple Approach for flexible and Stretchable Anti-icing Lubricant-Infused Tape. ACS Appl. Mater. Interfaces 13 (37), 45105–45115.
Carré, A., Mittal, K.L., 2009. Superhydrophobic Surfaces. VSP, Leiden; Boston.
Cassie, A.B.D., Baxter, S., 1944. Wettability of porous surfaces. Trans. Faraday Soc. 40 (0), 546–551.
Cebeci, T., Kafyeke, F., 2003. AIRCRAFT ICING. Annu. Rev. Fluid Mech. 35 (1), 11–21.
Cerman, Z., Striffler, B.F., Barthlott, W., 2009. Dry in the Water: The Superhydrophobic Water Fern Salvinia – A Model for Biomimetic Surfaces. In: Gorb, S.N. (Ed.), Functional Surfaces in Biology: Little Structures with Big Effects Volume 1. Springer Netherlands, Dordrecht, pp. 97–111.
Chaudhury, M.K., Whitesides, G.M., 1992. How to make Water Run Uphill. Science 256 (5063), 1539–1541.
Cheeseman, S., Owen, S., Truong, V.K., Meyer, D., Ng, S.H., Vongsvivut, J., Linklater, D., Tobin, M.J., Werner, M., Baulin, V.A., Luque, P., Marchant, R., Juodkazis, S., Crawford, R.J., Ivanova, E.P., 2018. Pillars of Life: is there a Relationship between Lifestyle Factors and the Surface Characteristics of Dragonfly Wings? ACS Omega 3 (6), 6039–6046.
Chen, M.-Y., Jia, Z.-H., Zhang, T., Fei, Y.-Y., 2018. Self-transport of underwater bubbles on a microholed hydrophobic surface with gradient wettability. Soft Matter 14 (36), 7462–7468.
Cheng, C.T., To, S, Zhang, G., 2020. Characterization of intermediate wetting states on micro-grooves by water droplet contact line. J. Ind. Eng. Chem. 91, 69–78.
Chieng, B.W., Ibrahim, N.A., Ahmad Daud, N., Talib, Z.A., 2019. Chapter 8 - Functionalization of Graphene Oxide via Gamma-Ray Irradiation for Hydrophobic Materials. In: Rashid, S.A., Raja Othman, R.N.I., Hussein, M.Z. (Eds.), Synthesis, Technology and Applications of Carbon Nanomaterials. Elsevier, pp. 177–203.
Chowdhury, I.U., Mahapatra, P.S., Sen, A.K., 2021a. Shape evolution of drops on surfaces of different wettability gradients. Chem. Eng. Sci. 229, 116136.
Chowdhury, I.U., Mahapatra, P.S., Sen, A.K., Pattamatta, A., Tiwari, M.K., 2021b. Autonomous transport and splitting of a droplet on an open surface. Phys. Rev. Fluid. 6 (9), 094003.
Chu, F., Wen, D., Wu, X., 2018. Frost Self-Removal Mechanism during Defrosting on Vertical Superhydrophobic Surfaces: Peeling off or jumping off. Langmuir 34 (48), 14562–14569.
Chu, F., Gao, S., Zhang, X., Wu, X., Wen, D., 2019a. Droplet re-icing characteristics on a superhydrophobic surface. Appl. Phys. Lett. 115 (7), 073703.
Chu, F., Zhang, X., Li, S., Jin, H., Zhang, J., Wu, X., Wen, D., 2019b. Bubble formation in freezing droplets. Phys. Rev. Fluid. 4 (7), 071601.
Chu, F., Luo, J., Hao, C., Zhang, J., Wu, X., Wen, D., 2020. Directional Transportation of Impacting Droplets on Wettability-Controlled Surfaces. Langmuir 36 (21), 5855–5862.
Cole, J., Sand, W., 1991. Statistical study of aircraft icing accidents. In: 29th Aerospace Sciences Meeting. Aerospace Sciences Meetings. American Institute of Aeronautics and Astronautics.
Crawford, R., Ivanova, E., 2015. Natural Superhydrophobic Surfaces, pp. 7–25.
Cui, W., Pakkanen, T.A., 2020. Icephobic performance of one-step silicone-oil-infused slippery coatings: Effects of surface energy, oil and nanoparticle contents. J. Colloid Interface Sci. 558, 251–258.
Czernkovich, N., 2004. Understanding in-flight icing. In: Transport Canada Aviation Safety Seminar, pp. 1–21.
Dai, B., Li, K., Shi, L., Wan, X., Liu, X., Zhang, F., Jiang, L., Wang, S., 2019. Bioinspired Janus Textile with Conical Micropores for Human Body Moisture and thermal Management. Adv. Mater. 31 (41), 1904113.
Daniel, S., Chaudhury, M.K., Chen, J.C., 2001. Fast Drop Movements Resulting from the phase Change on a Gradient Surface. Science 291 (5504), 633–636.
Darmanin, T., Guittard, F., 2015. Superhydrophobic and superoleophobic properties in nature. Mater. Today 18 (5), 273–285.
Decker, E.L., Frank, B., Suo, Y., Garoff, S., 1999. Physics of contact angle measurement. Colloids Surf. A Physicochem. Eng. Asp. 156 (1), 177–189.
Deng, S., Shang, W., Feng, S., Zhu, S., Xing, Y., Li, D., Hou, Y., Zheng, Y., 2017. Controlled droplet transport to target on a high adhesion surface with multi-gradients. Sci. Rep. 7 (1), 45687.
Dietz, C., Rykaczewski, K., Fedorov, A.G., Joshi, Y., 2010. Visualization of droplet departure on a superhydrophobic surface and implications to heat transfer enhancement during dropwise condensation. Appl. Phys. Lett. 97 (3), 033104.
Dou, W., Wu, J., Gu, T., Wang, P., Zhang, D., 2018. Preparation of super-hydrophobic micro-needle CuO surface as a barrier against marine atmospheric corrosion. Corros. Sci. 131, 156–163.
Dussan, V.E.B., Chow, R.T.-P., 1983. On the ability of drops or bubbles to stick to non-horizontal surfaces of solids. J. Fluid Mech. 137, 1–29.
Elbahri, M., Paretkar, D., Hirmas, K., Jebril, S., Adelung, R., 2007. Anti-Lotus effect for Nanostructuring at the Leidenfrost Temperature. Adv. Mater. 19 (9), 1262–1266.
Feng, L., Li, S., Li, Y., Li, H., Zhang, L., Zhai, J., Song, Y., Liu, B., Jiang, L., Zhu, D., 2002. Super-Hydrophobic Surfaces: from Natural to Artificial. Adv. Mater. 14 (24), 1857–1860.
Feng, X.-Q., Gao, X., Wu, Z., Jiang, L., Zheng, Q.-S., 2007. Superior Water Repellency of Water Strider Legs with Hierarchical Structures: experiments and Analysis. Langmuir 23 (9), 4892–4896.
Feng, X., Zhang, X., Tian, G., 2022. Recent advances in bioinspired superhydrophobic ice-proof surfaces: challenges and prospects. Nanoscale 14 (16), 5960–5993.
Fortin, G., Perron, J., 2009. Spinning Rotor Blade Tests in Icing Wind Tunnel. In: 1st AIAA Atmospheric and Space Environments Conference. Fluid Dynamics and Co-located Conferences. American Institute of Aeronautics and Astronautics.
Gao, X., Jiang, L., 2004. Water-repellent legs of water striders. Nature 432 (7013), 36.
Gao, Y., Wang, J., Xia, W., Mou, X., Cai, Z., 2018. Reusable Hydrophilic–Superhydrophobic Patterned Weft Backed Woven fabric for High-Efficiency Water-Harvesting Application. ACS Sustain. Chem. Eng. 6 (6), 7216–7220.
Göhl, J., Mark, A., Sasic, S., Edelvik, F., 2018. An immersed boundary based dynamic contact angle framework for handling complex surfaces of mixed wettabilities. Int. J. Multiphase Flow 109, 164–177.
Golovin, K., Kobaku, S.P.R., Lee, D.H., DiLoreto, E.T., Mabry, J.M., Tuteja, A., 2016. Designing durable icephobic surfaces. Sci. Adv. 2 (3), e1501496.
Good, R.J., 1952. A Thermodynamic Derivation of Wenzel's Modification of Young's Equation for Contact Angles; together with a Theory of Hysteresis1. J. Am. Chem. Soc. 74 (20), 5041–5042.
Greenspan, H.P., 1978. On the motion of a small viscous droplet that wets a surface. J. Fluid Mech. 84 (1), 125–143.
Guo, P., Zheng, Y., Wen, M., Song, C., Lin, Y., Jiang, L., 2012. Icephobic/Anti-Icing Properties of Micro/Nanostructured Surfaces. Adv. Mater. 24 (19), 2642–2648.
Gurera, D., Bhushan, B., 2019. Multistep Wettability Gradient on Bioinspired Conical Surfaces for Water Collection from fog. Langmuir 35 (51), 16944–16947.
Hall, A.J., 1966. Textile Finishing. Finissage des Textiles.
Hann, R., Johansen, T.A., 2021. UAV icing: the influence of airspeed and chord length on performance degradation. Aircr. Eng. Aerosp. Technol. 93 (5), 832–841.
Heinilä, E., 2021. Long-Term Correction of Icing Losses Based on Operational Data from Three Wind Farms in Finland. Aalto University, p. 39.
Hoque, M.J., Yan, X., Keum, H., Li, L., Cha, H., Park, J.K., Kim, S., Miljkovic, N., 2020. High-Throughput Stamping of Hybrid Functional Surfaces. Langmuir 36 (21), 5730–5744.
Hou, Y., Yu, M., Shang, Y., Zhou, P., Song, R., Xu, X., Chen, X., Wang, Z., Yao, S., 2018. Suppressing Ice Nucleation of Supercooled Condensate with Biphilic Topography. Phys. Rev. Lett. 120 (7), 075902.
Hu, C., Chen, W., Li, T., Ding, Y., Yang, H., Zhao, S., Tsiwah, E.A., Zhao, X., Xie, Y., 2018. Constructing non-fluorinated porous superhydrophobic SiO2-based films with robust mechanical properties. Colloids Surf. A Physicochem. Eng. Asp. 551, 65–73.
Huang, J., Wang, L., He, K., 2022. Three-dimensional study of double droplets impact on a wettability-patterned surface. Comput. Fluids. 248, 105669.
Ignatyev, D.I., Khrabrov, A.N., Kortukova, A.I., Alieva, D.A., Sidoryuk, M.E., Bazhenov, S.G., 2020. Interplay of unsteady aerodynamics and flight dynamics of transport aircraft in icing conditions. Aerosp. Sci. Technol. 104, 105914.
Ivanova, E.P., Hasan, J., Webb, H.K., Truong, V.K., Watson, G.S., Watson, J.A., Baulin, V. A., Pogodin, S., Wang, J.Y., Tobin, M.J., Löbbe, C., Crawford, R.J., 2012. Natural bactericidal surfaces: mechanical rupture of Pseudomonas aeruginosa cells by cicada wings. Small 8 (16), 2489–2494.
Ivanova, E.P., Hasan, J., Webb, H.K., Gervinskas, G., Juodkazis, S., Truong, V.K., Wu, A. H.F., Lamb, R.N., Baulin, V.A., Watson, G.S., Watson, J.A., Mainwaring, D.E., Crawford, R.J., 2013a. Bactericidal activity of black silicon. Nat. Commun. 4 (1), 2838.
Ivanova, E.P., Nguyen, S.H., Webb, H.K., Hasan, J., Truong, V.K., Lamb, R.N., Duan, X., Tobin, M.J., Mahon, P.J., Crawford, R.J., 2013b. Molecular organization of the nanoscale surface structures of the dragonfly Hemianax papuensis wing epicuticle. PLoS One 8 (7), e67893.
Ivanović, L., Vencl, A., Stojanović, B., Marković, B., 2018. Biomimetics Design for Tribological Applications. Tribol. Ind. 40 (3), 448–456.
Ji, T., Pan, Y., Shao, Y., He, B., Wen, B., 2021. Lateral Drop Rebound on a Hydrophobic and Chemically Heterogeneous Surface. Langmuir 37 (23), 6905–6914.
Jiang, X., Zhuo, Y., Wang, P., Yang, M., Liao, Y., Chen, B., 2023. The Perspectives of Hydrophobic Coatings for Mitigating Icing on Atmospheric Structures. Coatings.
Jin, Z., Wang, Z., Sui, D., Yang, Z., 2016. The impact and freezing processes of a water droplet on different inclined cold surfaces. Int. J. Heat Mass Transf. 97, 211–223.
Jokinen, V., Sainiemi, L., Franssila, S., 2008. Complex Droplets on Chemically Modified Silicon Nanograss. Adv. Mater. 20 (18), 3453–3456.

Jung, S., Tiwari, M.K., Doan, N.V., Poulikakos, D., 2012. Mechanism of supercooled droplet freezing on surfaces. Nat. Commun. 3 (1), 615.
Kalikmanov, V.I., 2013. Classical Nucleation Theory. In: Kalikmanov, V.I. (Ed.), Nucleation Theory. Springer Netherlands, Dordrecht, pp. 17–41.
Kang, Z., Li, W., 2017. Facile and fast fabrication of superhydrophobic surface on magnesium alloy by one-step electrodeposition method. J. Ind. Eng. Chem. 50, 50–56.
Kaul, R.B., 1976. Anatomical observations on floating leaves. Aquat. Bot. 2, 215–234.
Khojasteh, D., Manshadi, M.K.D., Mousavi, S.M., Sotoudeh, F., Kamali, R., Bordbar, A., 2020. Electrically modulated droplet impingement onto hydrophilic and (super) hydrophobic solid surfaces. J. Braz. Soc. Mech. Sci. Eng. 42 (4), 153.
Kim, D.-H., Lee, D.-H., 2019. Effect of irradiation on the surface morphology of nanostructured superhydrophobic surfaces fabricated by ion beam irradiation. Appl. Surf. Sci. 477, 154–158.
Kim, J.H., Kim, M.J., Lee, B., Chun, J.M., Patil, V., Kim, Y.-S., 2020. Durable ice-lubricating surfaces based on polydimethylsiloxane embedded silicone oil infused silica aerogel. Appl. Surf. Sci. 512, 145728.
Kind, R.J., Potapczuk, M.G., Feo, A., Golia, C., Shah, A.D., 1998. Experimental and computational simulation of in-flight icing phenomena. Prog. Aerosp. Sci. 34 (5), 257–345.
Koch, K., Barthlott, W., 1893. 2009. Superhydrophobic and superhydrophilic plant surfaces: an inspiration for biomimetic materials. Philosophical transactions of the Royal Society a: Mathematical. Phys. Eng. Sci. 367, 1487–1509.
Koch, K., Ensikat, H.-J., 2008. The hydrophobic coatings of plant surfaces: Epicuticular wax crystals and their morphologies, crystallinity and molecular self-assembly. Micron 39 (7), 759–772.
Kulinich, S.A., Farzaneh, M., 2009. Ice adhesion on super-hydrophobic surfaces. Appl. Surf. Sci. 255 (18), 8153–8157.
Kulinich, S.A., Farzaneh, M., 2011. On ice-releasing properties of rough hydrophobic coatings. Cold Reg. Sci. Technol. 65 (1), 60–64.
Lai, Y.-H., Yang, J.-T., Shieh, D.-B., 2010. A microchip fabricated with a vapor-diffusion self-assembled-monolayer method to transport droplets across superhydrophobic to hydrophilic surfaces. Lab Chip 10 (4), 499–504.
Langley, K.R., Li, E.Q., Vakarelski, I.U., Thoroddsen, S.T., 2018. The air entrapment under a drop impacting on a nano-rough surface. Soft Matter 14 (37), 7586–7596.
Laroche, A., Bottone, D., Seeger, S., Bonaccurso, E., 2021. Silicone nanofilaments grown on aircraft alloys for low ice adhesion. Surf. Coat. Technol. 410, 126971.
Launay, G., Sadullah, M.S., McHale, G., Ledesma-Aguilar, R., Kusumaatmaja, H., Wells, G.G., 2020. Self-propelled droplet transport on shaped-liquid surfaces. Sci. Rep. 10 (1), 14987.
Lengaigne, J., Bousser, E., Brown, S., Xing, P., Turcot, F., Dolatabadi, A., Martinu, L., Klemberg-Sapieha, J.E., 2020. In situ ice growth kinetics on water-repellent coatings under atmospheric icing conditions. Surf. Coat. Technol. 399, 126136.
Li, J., Tian, X., Perros, A.P., Franssila, S., Jokinen, V., 2014. Self-Propelling and Positioning of Droplets using Continuous Topography Gradient Surface. Adv. Mater. Interfaces 1 (3), 1400001.
Li, Q., Yu, Y., Zhou, P., Yan, H., 2017a. Droplet migration on hydrophobic–hydrophilic hybrid surfaces: a lattice Boltzmann study. RSC Adv. 7 (24), 14701–14708.
Li, S., Huang, J., Chen, Z., Chen, G., Lai, Y., 2017b. A review on special wettability textiles: theoretical models, fabrication technologies and multifunctional applications. J. Mater. Chem. A 5 (1), 31–55.
Liu, Y., Hu, H., 2018. An experimental investigation on the unsteady heat transfer process over an ice accreting airfoil surface. Int. J. Heat Mass Transf. 122, 707–718.
Liu, Y., Li, L., Li, H., Hu, H., 2018. An experimental study of surface wettability effects on dynamic ice accretion process over an UAS propeller model. Aerosp. Sci. Technol. 73, 164–172.
Lockey, K.H., 1988. Lipids of the insect cuticle: origin, composition and function. Comparat. Biochem. Physiol. Part B: Comparat. Biochem. 89 (4), 595–645.
Lomga, J., Varshney, P., Nanda, D., Satapathy, M., Mohapatra, S.S., Kumar, A., 2017. Fabrication of durable and regenerable superhydrophobic coatings with excellent self-cleaning and anti-fogging properties for aluminium surfaces. J. Alloys Compd. 702, 161–170.
Luo, L., Wang, X.-P., Cai, X.-C., 2017. An efficient finite element method for simulation of droplet spreading on a topologically rough surface. J. Comput. Phys. 349, 233–252.
Macner, A.M., Daniel, S., Steen, P.H., 2014. Condensation on Surface Energy Gradient Shifts Drop size distribution toward Small Drops. Langmuir 30 (7), 1788–1798.
Marín, A.G., Enríquez, O.R., Brunet, P., Colinet, P., Snoeijer, J.H., 2014. Universality of Tip Singularity Formation in Freezing Water Drops. Phys. Rev. Lett. 113 (5), 054301.
Memon, H., Wang, J., Hou, X., 2023. Interdependence of Surface Roughness on Icephobic Performance: A Review, Materials.
Meng, Z., Zhang, P., 2020. Dynamic propagation of ice-water phase front in a supercooled water droplet. Int. J. Heat Mass Transf. 152, 119468.
Mertaniemi, H., Jokinen, V., Sainiemi, L., Franssila, S., Marmur, A., Ikkala, O., Ras, R.H. A., 2011. Superhydrophobic Tracks for Low-Friction, Guided Transport of Water Droplets. Adv. Mater. 23 (26), 2911–2914.
Mikkelsen, K., McKnight, R., Ranaudo, R., Perkins, J.P., 1985. Icing flight research - aerodynamic effects of ice and ice shape documentation with stereo photography. In: 23rd Aerospace Sciences Meeting. Aerospace Sciences Meetings. American Institute of Aeronautics and Astronautics.
Mishchenko, L., Hatton, B., Bahadur, V., Taylor, J.A., Krupenkin, T., Aizenberg, J., 2010. Design of Ice-free Nanostructured Surfaces Based on Repulsion of Impacting Water Droplets. ACS Nano 4 (12), 7699–7707.
Mishchenko, L., Khan, M., Aizenberg, J., Hatton, B.D., 2013. Spatial Control of Condensation and Freezing on Superhydrophobic Surfaces with Hydrophilic Patches. Adv. Funct. Mater. 23 (36), 4577–4584.
Mittal, K.L., 2014. Contact Angle, Wettability and Adhesion, 2.
Moore, E.B., Molinero, V., 2011. Structural transformation in supercooled water controls the crystallization rate of ice. Nature 479 (7374), 506–508.
Mora, J., García, P., Muelas, R., Agüero, A., 2020. Hard Quasicrystalline Coatings Deposited by HVOF thermal Spray to Reduce Ice Accretion in Aero-Structures Components. Coatings 10 (3), 290.
Mousavi, S.M., Lee, B.J., 2022. Investigation of bubble structure in a microchannel under microgravity conditions: Effects of discontinuous wettability with dynamic contact angle. Acta Astronaut. 201, 394–400.
Mousavi, S.M., Roohi, E., 2023. On the effects of hybrid surface wettability on the structure of cavitating flow using implicit large eddy simulation. J. Taiwan Inst. Chem. Eng. 104828.
Mousavi, S.M., Sotoudeh, F., Lee, B.J., Paydari, M.-R., Karimi, N., 2022. Effect of hybrid wall contact angles on slug flow behavior in a T-junction microchannel: a numerical study. Colloids Surf. A Physicochem. Eng. Asp. 650, 129677.
Mousavi, S.M., Jarrahbashi, D., Lee, B.J., Karimi, N., Faroughi, S.A., 2023. Impact of hybrid surfaces on the droplet breakup dynamics in microgravity slug flow: a dynamic contact angle analysis. Phys. Fluids 35 (7), 072003.
Muhammed, M., Virk, M.S., 2023. Ice Accretion on Rotary-Wing Unmanned Aerial Vehicles&Mdash;a Review Study, Aerospace.
Neinhuis, C., Barthlott, W., 1997. Characterization and distribution of Water-repellent, Self-cleaning Plant Surfaces. Ann. Bot. 79 (6), 667–677.
Nilsson, M.A., Rothstein, J.P., 2012. Using sharp transitions in contact angle hysteresis to move, deflect, and sort droplets on a superhydrophobic surface. Phys. Fluids 24 (6), 062001.
Nishimoto, S., Bhushan, B., 2013. Bioinspired self-cleaning surfaces with superhydrophobicity, superoleophobicity, and superhydrophilicity. RSC Adv. 3 (3), 671–690.
Nouri, N.M., Bakhsh, M.S., Sekhavat, S., 2013. Analysis of shear rate effects on drag reduction in turbulent channel flow with superhydrophobic wall. J. Hydrodyn. 25 (6), 944–953.
Nuraje, N., Khan, W.S., Lei, Y., Ceylan, M., Asmatulu, R., 2013. Superhydrophobic electrospun nanofibers. J. Mater. Chem. A 1 (6), 1929–1946.
Ollivier, H., 1907. Recherches sur la capillarité. J. Phys. Theor. Appl. 6 (1), 757–782.
Onda, T., Shibuichi, S., Satoh, N., Tsujii, K., 1996. Super-Water-Repellent Fractal Surfaces. Langmuir 12 (9), 2125–2127.
Papadakis, M., Rachman, A., Wong, S.-C., Yeong, H.-W., Hung, K.E., Vu, G.T., Bidwell, C. S., 2007. Water Droplet Impingement on Simulated Glaze, Mixed, and Rime Ice Accretions.
Pavković-Lučić, S., Miličić, D., Lučić, L., 2012. Insect Hydrocarbons. Biology, Biochemistry, and Chemical Ecology edited by Gary J. Blomquist, Anne-Geneviève Bagnères. Insect Sci. 19 (6), 703–704.
Pérez-Díaz, J.L., Álvarez-Valenzuela, M.A., Rodríguez-Celis, F., 2016. Surface freezing of water. SpringerPlus 5 (1), 629.
Pierce, E., Carmona, F.J., Amirfazli, A., 2008. Understanding of sliding and contact angle results in tilted plate experiments. Colloids Surf. A Physicochem. Eng. Asp. 323 (1), 73–82.
Piscitelli, F., 2022. Characterization in Relevant Icing Conditions of two Superhydrophobic Coatings. Appl. Sci. 12 (8), 3705.
Piscitelli, F., Palazzo, S., De Nicola, F., 2023. Icing Wind Tunnel Test Campaign on a Nacelle Lip-Skin to Assess the effect of a Superhydrophobic Coating on Ice Accretion. Appl. Sci. 13 (8), 5183.
Pogodin, S., Hasan, J., Baulin, V.A., Webb, H.K., Truong, V.K., Phong Nguyen, T.H., Boshkovikj, V., Fluke, C.J., Watson, G.S., Watson, J.A., Crawford, R.J., Ivanova, E.P., 2013. Biophysical model of bacterial cell interactions with nanopatterned cicada wing surfaces. Biophys. J. 104 (4), 835–840.
Politovich, M.K., 2000. Predicting glaze or rime ice growth on airfoils. J. Aircr. 37 (1), 117–121.
Poots, G., Gent, R.W., Dart, N.P., Cansdale, J.T., 1776. 2000. Aircraft icing. Philosophical transactions of the Royal Society of London. Series a: Mathematical. Phys. Eng. Sci. 358, 2873–2911.
Pravinraj, T., Patrikar, R., 2019. A droplet actuation technique for a lab-on-chip device using partial wetting surface without external force. Sensors Actuators A Phys. 285, 482–490.
Qiu, R., Zhang, D., Wang, P., 2013. Superhydrophobic-carbon fibre growth on a zinc surface for corrosion inhibition. Corros. Sci. 66, 350–359.
Quetzeri-Santiago, M.A., Castrejón-Pita, A.A., Castrejón-Pita, J.R., 2019. The effect of Surface Roughness on the Contact Line and Splashing Dynamics of Impacting Droplets. Sci. Rep. 9 (1), 15030.
Rivero, P.J., Rodriguez, R.J., Larumbe, S., Monteserín, M., Martín, F., García, A., Acosta, C., Clemente, M.J., García, P., Mora, J., Agüero, A., 2020. Evaluation of Functionalized Coatings for the Prevention of Ice Accretion by using Icing Wind Tunnel Tests. Coatings 10 (7), 636.
Russo, A., Icardi, M., Elsharkawy, M., Ceglia, D., Asinari, P., Megaridis, C.M., 2020. Numerical simulation of droplet impact on wettability-patterned surfaces. Phys. Rev. Fluid. 5 (7), 074002.
Samuels, L., Kunst, L., Jetter, R., 2008. Sealing plant surfaces: cuticular wax formation by epidermal cells. Annu. Rev. Plant Biol. 59, 683–707.
Sarshar, M.A., Song, D., Swarctz, C., Lee, J., Choi, C.-H., 2018. Anti-Icing or Deicing: Icephobicities of Superhydrophobic Surfaces with Hierarchical Structures. Langmuir 34 (46), 13821–13827.
Schremb, M., Tropea, C., 2016. Solidification of supercooled water in the vicinity of a solid wall. Phys. Rev. E 94 (5), 052804.
Schroeder, T.B.H., Houghtaling, J., Wilts, B.D., Mayer, M., 2018. It's not a bug, It's a Feature: Functional Materials in Insects. Adv. Mater. 30 (19), 1705322.
Shang, X., Luo, Z., Bai, B., 2019. Droplets trapped by a wetting surface with chemical defects in shear flows. Chem. Eng. Sci. 195, 433–441.

Simpson, J.T., Hunter, S.R., Aytug, T., 2015. Superhydrophobic materials and coatings: a review. Rep. Prog. Phys. 78 (8), 086501.
Song, D., Song, B., Hu, H., Du, X., Ma, Z., 2015a. Contact angle and impinging process of droplets on partially grooved hydrophobic surfaces. Appl. Therm. Eng. 85, 356–364.
Song, D., Song, B., Hu, H., Du, X., Zhou, F., 2015b. Selectively splitting a droplet using superhydrophobic stripes on hydrophilic surfaces. Phys. Chem. Chem. Phys. 17 (21), 13800–13803.
Sotoudeh, F., Kamali, R., Mousavi, S.M., Karimi, N., Lee, B.J., Khojasteh, D., 2021. Understanding droplet collision with superhydrophobic-hydrophobic–hydrophilic hybrid surfaces. Colloids Surf. A Physicochem. Eng. Asp. 614, 126140.
Sotoudeh, F., Mousavi, S.M., Karimi, N., Lee, B.J., Abolfazli-Esfahani, J., Manshadi, M.K. D., 2023. Natural and synthetic superhydrophobic surfaces: a review of the fundamentals, structures, and applications. Alex. Eng. J. 68, 587–609.
Tourkine, P., Le Merrer, M., Quéré, D., 2009. Delayed Freezing on Water Repellent Materials. Langmuir 25 (13), 7214–7216.
Tripathy, A., Sen, P., Su, B., Briscoe, W.H., 2017. Natural and bioinspired nanostructured bactericidal surfaces. Adv. Colloid Interf. Sci. 248, 85–104.
Truong, V.K., Geeganagamage, N.M., Baulin, V.A., Vongsvivut, J., Tobin, M.J., Luque, P., Crawford, R.J., Ivanova, E.P., 2017. The susceptibility of Staphylococcus aureus CIP 65.8 and Pseudomonas aeruginosa ATCC 9721 cells to the bactericidal action of nanostructured Calopteryx haemorrhoidalis damselfly wing surfaces. Appl. Microbiol. Biotechnol. 101 (11), 4683–4690.
Ueda, E., Levkin, P.A., 2013. Emerging applications of Superhydrophilic-Superhydrophobic Micropatterns. Adv. Mater. 25 (9), 1234–1247.
Vukits, T., 2002. Overview and risk assessment of icing for transport category aircraft and components. In: 40th AIAA Aerospace Sciences Meeting & Exhibit. Aerospace Sciences Meetings. American Institute of Aeronautics and Astronautics.
Wang, F., Li, C., Lv, Y., Lv, F., Du, Y., 2010a. Ice accretion on superhydrophobic aluminum surfaces under low-temperature conditions. Cold Reg. Sci. Technol. 62 (1), 29–33.
Wang, L., Peng, B., Su, Z., 2010b. Tunable Wettability and Rewritable Wettability Gradient from Superhydrophilicity to Superhydrophobicity. Langmuir 26 (14), 12203–12208.
Wang, X., Sun, D.-L., Wang, X.-D., Yan, W.-M., 2019. Dynamics of droplets impacting hydrophilic surfaces decorated with a hydrophobic strip. Int. J. Heat Mass Transf. 135, 235–246.
Wang, F., Zhuo, Y., He, Z., Xiao, S., He, J., Zhang, Z., 2021. Dynamic Anti-Icing Surfaces (DAIS). Adv. Sci. 8 (21), 2101163.
Wang, L., Jiang, G., Zhu, D., Tian, Z., Chen, C., Hu, X., Peng, R., Li, D., Zhang, H., Zhao, H., Fan, P., Zhong, M., 2023. Self-driven droplet motions below their icing points. Small 2302339 n/a(n/a).
Watson, G.S., Cribb, B.W., Watson, J.A., 2010. How Micro/Nanoarchitecture Facilitates Anti-Wetting: an Elegant Hierarchical Design on the Termite Wing. ACS Nano 4 (1), 129–136.
Wendell, D.W., Patti, J., Montemagno, C.D., 2006. Using Biological Inspiration to Engineer Functional Nanostructured Materials. Small 2 (11), 1324–1329.
Wenzel, R.N., 1936. Resistance of solid surfaces to wetting by water. Ind. Eng. Chem. 28 (8), 988–994.
Wolfs, M., Darmanin, T., Guittard, F., 2013. Superhydrophobic Fibrous Polymers. Polym. Rev. 53 (3), 460–505.
Wu, H., Zhu, K., Cao, B., Zhang, Z., Wu, B., Liang, L., Chai, G., Liu, A., 2017. Smart design of wettability-patterned gradients on substrate-independent coated surfaces to control unidirectional spreading of droplets. Soft Matter 13 (16), 2995–3002.
Xiao, X., Li, S., Zhu, X., Xiao, X., Zhang, C., Jiang, F., Yu, C., Jiang, L., 2021. Bioinspired Two-Dimensional Structure with Asymmetric Wettability Barriers for Unidirectional and Long-Distance Gas Bubble delivery Underwater. Nano Lett. 21 (5), 2117–2123.
Xing, Y., Zhang, Y., Ding, S., Zheng, X., Xu, M., Cao, Y., Gui, X., 2020. Effect of surface roughness on the detachment between bubble and glass beads with different contact angles. Powder Technol. 361, 812–816.
Xu, X., 2016. Modified Wenzel and Cassie Equations for Wetting on Rough Surfaces. SIAM J. Appl. Math. 76 (6), 2353–2374.
Xu, X., Wang, D., Wang, X.-P., 2017. An efficient threshold dynamics method for wetting on rough surfaces. J. Comput. Phys. 330, 510–528.
Yang, Q., Zhu, Z., Tan, S., Luo, Y., Luo, Z., 2020. How Micro-/Nanostructure Evolution Influences Dynamic Wetting and Natural Deicing Abilities of Bionic Lotus Surfaces. Langmuir 36 (15), 4005–4014.
Yin, L., Zhu, L., Wang, Q., Ding, J., Chen, Q., 2011. Superhydrophobicity of Natural and Artificial Surfaces under Controlled Condensation Conditions. ACS Appl. Mater. Interfaces 3 (4), 1254–1260.
Yin, K., Du, H., Dong, X., Wang, C., Duan, J.-A., He, J., 2017. A simple way to achieve bioinspired hybrid wettability surface with micro/nanopatterns for efficient fog collection. Nanoscale 9 (38), 14620–14626.
Yuan, Z., Matsumoto, M., Kurose, R., 2020. Directional migration of an impinging droplet on a surface with wettability difference. Phys. Rev. Fluid. 5 (11), 113605.
Zhang, K., Wei, T., Hu, H., 2015. An experimental investigation on the surface water transport process over an airfoil by using a digital image projection technique. Exp. Fluids 56 (9), 173.
Zhang, M., Feng, S., Wang, L., Zheng, Y., 2016. Lotus effect in wetting and self-cleaning. Biotribology 5, 31–43.
Zhang, Z.A.L., Hu, H., Bai, X., Hu, H., 2021. An experimental study on the detrimental effects of deicing fluids on the performance of icephobic coatings for aircraft icing mitigation. Aerosp. Sci. Technol. 119, 107090.
Zhang, Y., Meng, N., Babar, A.A., Wang, X., Yu, J., Ding, B., 2021a. Multi-bioinspired and Multistructural Integrated Patterned Nanofibrous Surface for Spontaneous and Efficient fog Collection. Nano Lett. 21 (18), 7806–7814.
Zhang, Z., Ma, L., Liu, Y., Ren, J., Hu, H., 2021c. An experimental study of rain erosion effects on a hydro−/ice-phobic coating pertinent to Unmanned-Arial-System (UAS) inflight icing mitigation. Cold Reg. Sci. Technol. 181, 103196.
Zhou, X., Sun, Y., Liu, J., 2021. Designing Anti-Icing Surfaces by Controlling Ice Formation. Adv. Mater. Interfaces 8 (17), 2100327.
Zhu, J., Dai, X., 2019. A new model for contact angle hysteresis of superhydrophobic surface. AIP Adv. 9 (6), 065309.
Zhuo, Y., Chen, J., Xiao, S., Li, T., Wang, F., He, J., Zhang, Z., 2021. Gels as emerging anti-icing materials: a mini review. Mater. Horiz. 8 (12), 3266–3280.
Zou, L., Wang, H., Zhu, X., Chen, R., Ding, Y., Liao, Q., 2020. Maximum spread of droplets on chemically striped surfaces. AICHE J. 66 (1), e16774.